Constructing the crust along the Galapagos Spreading Center 91.3°–95.5°W: Correlation of seismic layer 2A with axial magma lens and topographic characteristics

T. M. Blacic,[1] G. Ito,[2] J. P. Canales,[3] R. S. Detrick,[3] and J. Sinton[2]

Received 5 March 2004; revised 2 July 2004; accepted 22 July 2004; published 21 October 2004.

[1] Multichannel seismic reflection data are used to infer crustal accretion processes along the intermediate spreading Galapagos Spreading Center. East of 92.5°W, we image a magma lens beneath the ridge axis that is relatively shallow (1.0–2.5 km below the seafloor) and narrow (~0.5–1.5 km, cross-axis width). We also image a thin seismic layer 2A (0.24–0.42 km) that thickens away from the ridge axis by as much as 150%. West of 92.7°W, the magma lens is deeper (2.5–4.5 km) and wider (0.7–2.4 km), and layer 2A is thicker (0.36–0.66 km) and thickens off axis by <40%. The positive correlation between layer 2A thickness and magma lens depth supports the interpretation of layer 2A as the extrusive volcanic layer with thickness controlled by the pressure on the magma lens and its ability to push magma to the surface. Our findings also suggest that narrower magma lenses focus diking close the ridge axis such that lava flowing away from the ridge axis will blanket older flows and thicken the extrusive crust off axis. Flow of lava away from the ridge axis is probably promoted by the slope of the axial bathymetric high, which is largest east of 92.5°W. West of ~94°W the "transitional" axial morphology lacks a prominent bathymetric high and layer 2A no longer thickens off axis. We detect no magma lens west of 94.7°W where a small axial valley appears. The above changes can be linked to the westward decrease in the magma and heat flux associated with the fading influence of the Galapagos hot spot on the Galapagos Spreading Center. *INDEX TERMS:* 3035 Marine Geology and Geophysics: Midocean ridge processes; 7220 Seismology: Oceanic crust; 0935 Exploration Geophysics: Seismic methods (3025); *KEYWORDS:* layer 2A, mid-ocean ridges, shallow melt lens

Citation: Blacic, T. M., G. Ito, J. P. Canales, R. S. Detrick, and J. Sinton (2004), Constructing the crust along the Galapagos Spreading Center 91.3°–95.5°W: Correlation of seismic layer 2A with axial magma lens and topographic characteristics, *J. Geophys. Res.*, *109*, B10310, doi:10.1029/2004JB003066.

1. Introduction

[2] The structure of the oceanic crust holds clues to the processes of crustal and lithospheric accretion at mid-ocean ridges. The standard layered model is based primarily on evidence from fast spreading ridges (~90–130 mm yr^{-1} full spreading rate), particularly the East Pacific Rise (EPR). The upper crust is seismically defined by a low-velocity (<2.5–5 km s^{-1}) upper layer 2A overlying a higher-velocity layer 2B (~5–6 km s^{-1}) [*Houtz*, 1976; *Houtz and Ewing*, 1976; *Vera et al.*, 1990; *Harding et al.*, 1993; *Christeson et al.*, 1994]. In addition to this layering in seismic velocity, some sections of mid-ocean ridges reveal a high-amplitude, relatively flat seismic reflector beneath the axis of seafloor spreading [e.g., *Herron et al.*, 1978, 1980; *Hale et al.*, 1982; *Morton and Sleep*, 1985; *Detrick et al.*, 1987; *Rohr et al.*, 1988; *Harding et al.*, 1989; *Vera et al.*, 1990; *Collier and Sinha*, 1990, 1992; *Kent et al.*, 1990, 1993b; *Mutter et al.*, 1995]. This reflector, which is not restricted to fast and superfast spreading ridges only, is most likely a thin sill of magma overlying a region of partially molten crust [*Sinton and Detrick*, 1992; *Hussenoeder et al.*, 1996; *Singh et al.*, 1998]. Most of the magma erupting probably passes through this magma lens [*Pan and Batiza*, 2003]; therefore an examination of correlations between the melt lens and layer 2A properties can help us understand accretionary processes.

[3] There are two main interpretations of the boundary between seismic layers 2A and 2B. The first is that it represents a porosity boundary within the extrusive crust resulting from fracturing or hydrothermal alteration [*McClain et al.*, 1985; *Becker et al.*, 1989; *Burnett et al.*, 1989; *Fisher et al.*, 1990; *Jacobson*, 1992; *Wilcock et al.*, 1992]. The second is that it is the boundary between the extrusive section and the sheeted dikes. The bulk of the

[1]Department of Geology, University of California at Davis, Davis, California, USA.
[2]School of Ocean and Earth Science and Technology, University of Hawaii, Honolulu, Hawaii, USA.
[3]Department of Geology and Geophysics, Woods Hole Oceanographic Institute, Woods Hole, Massachusetts, USA.

0148-0227/04/2004JB003066$09.00

evidence so far, including results of many recent seismic studies of fast spreading ridges [e.g., *Herron*, 1982; *Toomey et al.*, 1990; *Christeson et al.*, 1992, 1994, 1996; *Harding et al.*, 1993; *Vera and Diebold*, 1994; *Hooft et al.*, 1996, 1997; *Carbotte et al.*, 1997; *Hussenoeder et al.*, 2002a] and observations at Hess Deep [*Francheteau et al.*, 1992], supports the second hypothesis. East of our study area at the site of Deep Sea Drilling Project/Ocean Drilling Program Hole 504B lithological observations of the thickness of the extrusive layer and extrusive-dike transition zone (575 and 209 m, respectively [*Anderson et al.*, 1982]) are in agreement with estimates of layer 2A thickness from seismic experiments along the nearby Costa Rica Rift [*Buck et al.*, 1997]. An excellent summary of the major evidence supporting each interpretation is provided by *Bazin et al.* [2001].

[4] An important observation is that layer 2A often thickens with distance away from the ridge axis. This observation is thought to be caused by lava flowing and thickening the extrusive crust off axis. Such thickening is observed at fast and intermediate spreading rates [e.g., *Tivey and Johnson*, 1993; *Perfit et al.*, 1994; *Kent et al.*, 1994; *Mutter et al.*, 1995; *Carbotte et al.*, 1998; *Bazin et al.*, 2001; *Baran et al.*, 2003], but along the intermediate spreading Juan de Fuca Ridge (JdFR), the off-axis thickening shows large variability with some off-axis regions either thicker or thinner than on-axis regions [*Tivey and Johnson*, 1993; *McDonald et al.*, 1994; *Tivey*, 1994]. This structure may develop as a result of large temporal variations in magma supply with the extrusive layer thickening off axis during episodes of relatively high magmatic activity, and thinning due to extensional faulting during episodes of low magma supply [*Tivey*, 1994; *McDonald et al.*, 1994]. Thus simple off-axis thickening of the extrusive layer (and, by inference, seismic layer 2A) may occur along ridges with a relatively steady magma supply and minimal tectonic extension; the magnitude and off-axis extent of such thickening is likely to be controlled by factors such as the width of the neovolcanic zone and lava flow length [*Kappus et al.*, 1995; *Hooft et al.*, 1997; *Tolstoy et al.*, 1997; *Hussenoeder et al.*, 2002a; *Carbotte et al.*, 2000]. We will explore such factors in the present study of the Galapagos Spreading Center.

[5] The thickness of layer 2A also varies with distance along the ridge axis. For example, along the axis of the EPR, layer 2A tends to be thicker along deeper portions of the EPR and toward segment ends, where magma supply is hypothesized to be relatively low, and to be thinner along broader, shallower ridge sections where magma supply is thought to be the most robust [*Detrick et al.*, 1993; *Hooft et al.*, 1997; *Carbotte et al.*, 2000]. However, a clear relationship between other indicators of magma supply such as spreading rate is not evident, at least for the magnitude of variability represented by sections of the EPR not influenced by hot spots [*Tolstoy et al.*, 1997; *Hooft et al.*, 1997; *Babcock et al.*, 1998; *Carbotte et al.*, 2000]. What may be most fundamental in controlling the along-axis variability is revealed through a compilation by *Buck et al.* [1997] of data from several intermediate and fast spreading ridges showing that average layer 2A thickness on the ridge axis tends to increase with average magma lens depth. *Buck et al.* [1997] attribute this correlation to a balance between the crustal pressure on the magma lens and the hydrostatic head required to build an extrusive pile.

[6] If layer 2A thickening is caused by off-axis lava flows then we can hypothesize a correlation with axial topography, which might influence how far lava flows away from the ridge axis, as well as the width of the axial magma lens, which might determine how far off axis eruptions are likely to occur. In addition, an examination of correlations between magma lens properties and extrusive processes at the ridge axis could help us to understand the effects of variations in magma supply on the construction of the shallow oceanic crust. To date, no study has examined a setting in which large variations in axial morphology and magma lens properties correlate, and thus where their potential influences on layer 2A can be fully explored. One setting where these types of correlations could be found is along a ridge influenced by a hot spot.

[7] The Galapagos Spreading Center (GSC) near the Galapagos hot spot (Figure 1) is an ideal setting in which to test some of the proposed mechanisms for the construction of the shallow crust at mid-ocean ridges. Along the section of the western GSC closest to the hot spot (92.5°W–91°W), the crust is anomalously thick (7.5–8 km) [*Canales et al.*, 2002] and the ridge axis lies along a prominent axial topographic high, resembling that of the EPR [*Canales et al.*, 1997; *Detrick et al.*, 2002; *Sinton et al.*, 2003] (Figure 2). Farther away from the hot spot to the west, the crust thins and the axial high diminishes until ~95.5°W where the crust approaches a thickness of ~5.5 km and the ridge axis develops an axial valley like a smaller-scale version of the Mid-Atlantic Ridge. Between ~92.5°W and ~95°W, axial morphology is mostly transitional, with faulted terrain displaying neither an axial topographic high nor a valley. If magma supply and axial morphology control the characteristics of magma lenses and layer 2A, then the GSC is an excellent place to quantify such effects. Also, the GSC is an intermediate rate spreading ridge with a full spreading rate that changes by only ±5% in our study region (55 mm yr^{-1} at 91°W to 49 mm yr^{-1} at 95°W) [*DeMets et al.*, 1990]. We can thus examine how changes in crustal structure depend on long-term changes in magma supply and axial morphology, largely independent of changes in spreading rate.

[8] In this paper, we report findings of multichannel seismic (MCS) and bathymetry surveys completed as part of the Galapagos Plume–Ridge Interaction Multidisciplinary Experiment (G-PRIME) on board the R/V *Maurice Ewing*. Specific questions this paper will address include (1) how do characteristics of axial magma lens and topography relate to variations in layer 2A, (2) what controls on-axis thickness of layer 2A, and (3) what controls the amplitude and width of off-axis thickening of layer 2A.

2. Data Collection and Processing

2.1. MCS Data Acquisition and Processing

[9] A map of the MCS survey area is shown in Figure 2. In just over 8 days of surveying we collected reflection data over ~86% of the length of the ridge between ~95.5° and 91.25°W with nearly 100% coverage east of 94.5°W. We also obtained 16 cross-axis lines that extended at least 10 km

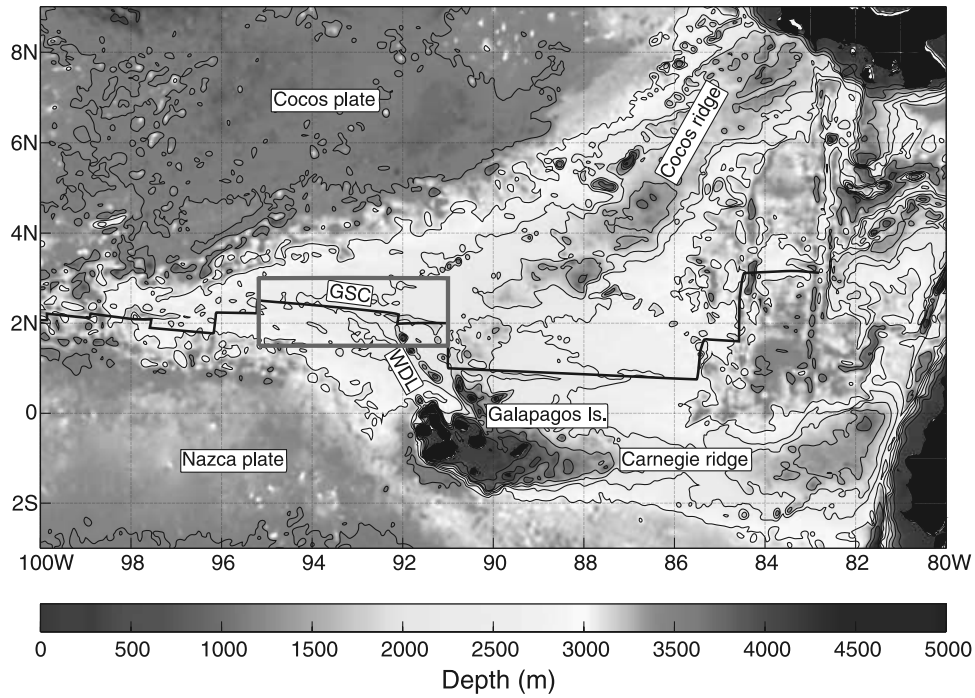

Figure 1. Map of the Galapagos region in the western equatorial Pacific. The MCS survey of the Galapagos Plume–Ridge Interaction Multidisciplinary Experiment (G-PRIME) focused on the western Galapagos Spreading Center (GSC) indicated by the green box. Black lines indicate location of ridge segments and transform faults. WDL is the Wolf-Darwin lineament. Contours are every 500 m. (After *Canales et al.* [2002], reprinted with permission from Elsevier Science.) See color version of this figure at back of this issue.

north and south of the ridge axis. The array of 10 air guns (4438 cubic inches, 72.7 L) was shot at an interval of 15 s with a 50-ms randomization window to minimize noise from consecutive shots. The shot interval and ship speed of ~4.5 knots (~8.3 km h^{-1}) resulted in shot spacing of 35–38 m. We used the Ewing's 6.1-km-long, 480-channel Syntrak streamer resulting in six, 80-fold reflection point gathers every shot. The entire MCS survey included ~40,500 shots and ~240,000 reflection points.

[10] Processing of the MCS data was carried out using the program package SIOSEIS (P. Henkart, http://sioseis.ucsd.edu). While on board, we performed near-real-time brute stacks, which assisted in the design of the later parts of the survey. Postcruise processing (summarized in Table 1) involved resorting the data into common midpoint (CMP) gathers muting, velocity analysis, filtering, and stacking. The focus of our processing was on three interfaces: the seafloor, the wide-angle arrival from the base of layer 2A, and the axial magma lens reflector (reflections from the base of the crust were only detected away from the ridge axis [see *Canales et al.*, 2002]).

[11] To identify the pertinent arrivals in CMP gathers and to design trace mutes, we constructed constant offset stacks by summing up to 200 consecutive CMP gathers. Trace mutes were designed to include the shallow, far-offset, layer 2A energy while excluding traces that experienced excessive stretching due to normal moveout. Because the signal from the magma lens reflector was confined to near-offset traces, we removed midoffset to far-offset data for travel times approximately ±0.5 s from the magma lens (see Figure 3). In all cases we kept only the nearest 3–4 km of the streamer (40–60 fold CMPs).

[12] Figure 3 shows examples of stacked CMP gathers from two along-axis lines, one far from the hot spot (~93.96°W, line AA2, Figure 3a) and one near the hot spot (~91.50°W, line AA3, Figure 3b). Arrivals from the base of layer 2A are evident just below the seafloor event at offsets of ~2.5–4 km and ~2–3 km, in Figures 3a and 3b, respectively. Arrivals from the base of layer 2A at far offsets are also seen in data for the EPR [e.g., *Harding et al.*, 1993; *Vera and Diebold*, 1994; *Christeson et al.*, 1996; *Hussenoeder et al.*, 1996, 2002a]. The axial magma lens reflector is strongest in the near offsets, as expected for a lens that is primarily composed of melt with few or no crystals [*Singh et al.*, 1998].

[13] We determined stacking velocities by applying normal moveout to individual CMP gathers at different (constant) velocities. For each interface, we chose the velocity that yielded the highest amplitude signal and interpolated velocities linearly between the interfaces. As shown by *Harding et al.* [1993] and *Kent et al.* [1993b], the sharp velocity gradient near the base of layer 2A produces sharp turning refractions at far offsets that mimic reflections. Stacking these arrivals as reflections produces an interface in stacked images, which approximately follows the base of layer 2A (base of the sharp velocity gradient) [*Harding et al.*, 1993].

[14] Cross-axis lines underwent the same processing scheme plus finite difference time migration. Three migration velocity profiles were created for each cross-axis line:

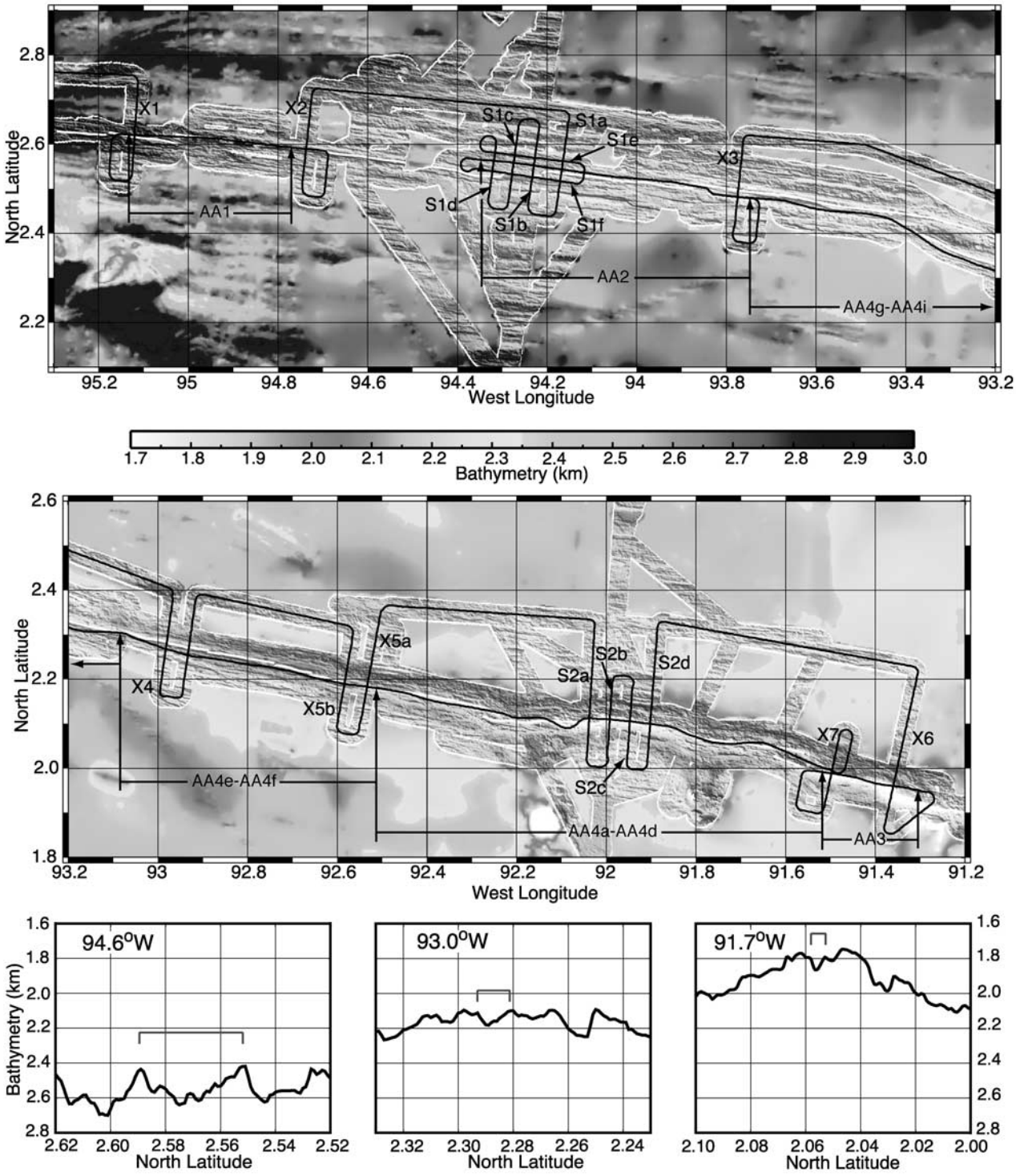

Figure 2. (top and middle) Bathymetry maps of the western Galapagos Spreading Center showing the location of the multichannel seismic reflection lines. (bottom) Bathymetry profiles showing cross sections of the ridge axis at 94.6°W, 93.0°W, and 91.7°W. A prominent axial high exists east of ~92.5°W. From ~92.7° to 95.3°W the ridge axis shows transitional topography lacking both an axial high and an axial valley. Red brackets indicate width of axial trough. See color version of this figure at back of this issue.

one at the axis and one on each flank. At the axis, migration velocities were chosen at the seafloor, at the base of layer 2A and at the magma lens reflector. On the flanks, migration velocities were picked at the seafloor and at the base of layer 2A only. Constant velocity migrations were used to select the velocities that best collapsed the diffractions at each interface without overmigrating. For a few survey lines where the seafloor was relatively rough (lines S1a–S1d,

Table 1. Processing Sequence and Parameters

Parameter	Processing Sequence
Geometry	CMP gather (80-fold, 6.25 m CMP interval)
Dip moveout (DMO, for lines with rough topography)	sort traces by range normal moveout (NMO, moveout velocity of 1500 m/s) DMO sort traces back to CMP remove NMO (1500 m/s)
Stacking	band-pass filter (5–40 Hz, 24 dB drop per octave) velocity analysis every 66–200 CMP NMO mute (stretch and surgical) stack
Time migration (for cross-axis lines)	band-pass filter (5–40 Hz, 24 dB drop per octave) mute from water multiple migration velocity analysis on-axis and on either flank finite difference 45° algorithm (3 velocity-depth profiles per line)
Display	band-pass filter (6–15 Hz, 15 dB drop per octave) mute to seafloor and from water multiple exponential gain

X3, and X4 toward the western end of the survey area), we also applied exact log dip move out [*Liner*, 1990] prior to muting and stacking to improve the imaging of steeply dipping shallow interfaces.

[15] In along-axis profiles of MCS stacks (Figure 4), reflections from the base of layer 2A can be seen ~0.3 to 0.5 s two-way travel time (TWTT) below the seafloor (unless otherwise noted, TWTT is measured from the seafloor), and the axial magma lens can be seen ~0.7–1.0 s TWTT. In the cross-axis lines (Figure 5), the axial magma lens is visible directly below the ridge axis at ~0.7 to 1.0 s TWTT. We estimate our error in picking the base of layer 2A and the axial magma lens, to be ±0.035 s TWTT and ±0.032 s TWTT, respectively.

2.2. Modeling Refractions for Layer 2 Velocity Structure

[16] Quantifying the thickness of layer 2A and the depth to the magma lens requires constraints on the velocity structure of the upper crust. To place these constraints, we analyzed common shot gathers at three locations on the ridge axis where the streamer lay above relatively flat seafloor and recorded a high-amplitude event from the bottom of layer 2A: 91.47°W, 92.32°W, and 94.01°W. Five consecutive shot gathers were stacked together and picks were made of the seafloor reflection (e.g., Figure 6b, open circles) and rays turning near the top of layer 2B (Figure 6b, solid circles). Near the hot spot where the seafloor was shallower, we imaged arrivals of rays turning in the steep velocity gradient at the base of layer 2A where they emerged before the seafloor in the far offsets (Figure 6b, gray bar). One-dimensional velocity profiles were derived by modeling the above arrivals with the ray tracing software RAYINVR [*Zelt and Smith*, 1992]. Following *Harding et al.* [1993] and *Hussenoeder et al.* [2002a] we define the bottom of layer 2A to correspond to the base of the steep velocity gradient between the low-velocity surface layer and the higher-velocity layer 2B. For the lower portion of the

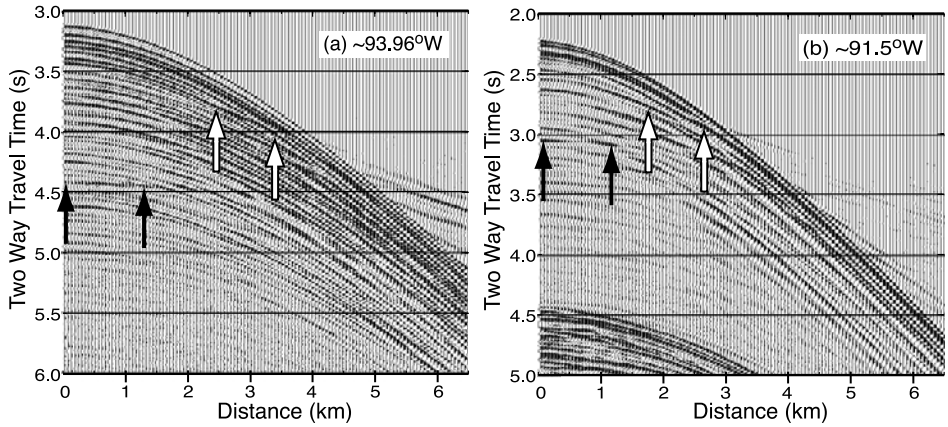

Figure 3. Example constant offset stacks from along-axis multichannel seismic survey lines. Stacks are plotted with a band-pass filter (5–20 Hz) and exponential gain function. Every fourth trace is shown. (a) Constant offset stack from ~93.96°W. The relatively flat axial magma lens reflector (above the black arrows) can be seen just above 4.5 s at near offsets. The layer 2A arrivals (above the white arrows) can be seen between ~3.8 and 4.1 s at middle offsets (~2.5 to ~3.5 km). (b) Constant offset stack from ~91.5°W. The axial magma lens reflector can be seen just below 3.0 s at near offsets. The layer 2A arrivals can be seen between ~2.7 and ~3.0 s at middle offsets.

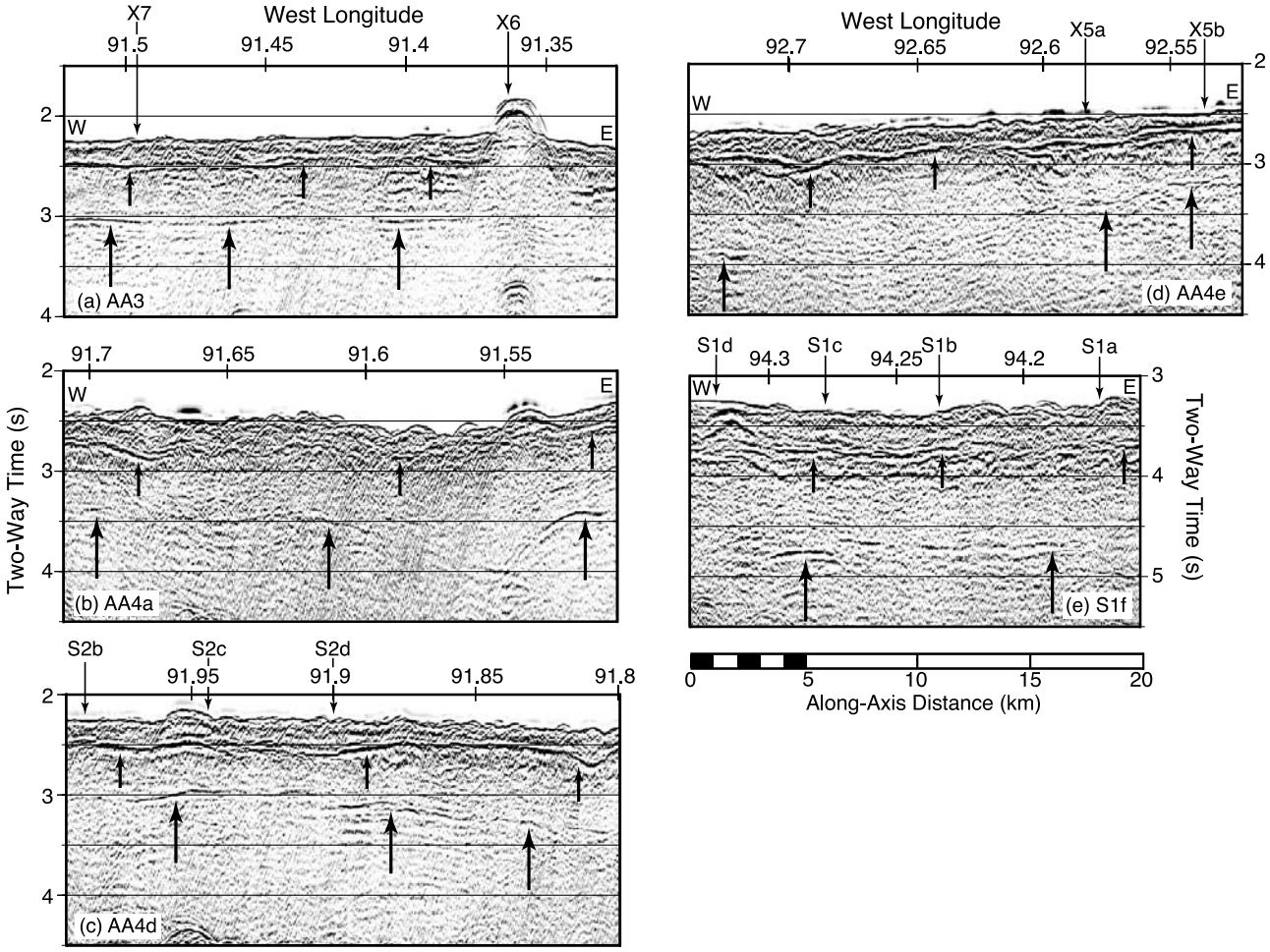

Figure 4. Example stacks of along-axis MCS profiles. Crossing lines are labeled and marked with downward pointing arrows. Large upward pointing arrows indicate some locations of the axial magma lens reflector. Small upward pointing arrows indicate some locations of the layer 2A seismic event. Processing is given in Table 1. (a) Closest to the hot spot, the axial magma lens is shallow, layer 2A is thin, and the seafloor topography is smooth (line AA3). There is an unidentified but strong reflector below 3.5 s two-way time in the easternmost part of this line where we were well north of the axis. (b) Moving westward, the axial magma lens becomes more discontinuous but remains shallow, layer 2A appears rougher but is still thin, and the seafloor topography becomes rougher (line AA4a). A small overlap basin was crossed in this region (~91.55° to ~91.65°W) resulting in a sharp dip in the apparent depth of the axial magma lens and imaging of two possible magma lens reflectors in the easternmost ~5 km. (c) West of the small overlap basin, the axial magma lens is fairly continuous and shallow (line AA4c). Layer 2A is also more continuous and thin but does not follow topography. (d) In the region spanning the disappearance of the axial high, deepening of the axial magma lens, and thickening of layer 2A (line AA4e) the axial magma lens is less continuous, but layer 2A remains bright and continuous although with a more complicated structure. (e) Where we observe the westernmost extent of the axial magma lens in our data (line S1f) the axial magma lens is deep, and layer 2A is thick and less continuous.

models, velocities were constrained to be in agreement with G-PRIME seismic refraction results [*Canales et al.*, 2002]. Best fitting velocity profiles were found by trial and error; velocity profiles were adjusted after each model run until a good fit was achieved. At each location, we obtained a good fit to the shot data from one to four different velocity-depth profiles. The differences between these profiles define the uncertainty of each fit.

[17] For each of the best fitting velocity profiles, we calculated a root-mean-square (RMS) velocity for layer 2A. Where we were able to include arrivals from rays turning in layer 2A (at 91.47°W and 92.32°W) the error in the RMS velocity for layer 2A is estimated to be ±0.17 km s^{-1} based on the standard deviation of the best fitting models. Results from 94.01°W were not used in calculating a mean RMS velocity for layer 2A because without picks from rays turning in the steep velocity gradient at the base of layer 2A we could not constrain both the thickness and velocity of layer 2A in our models. RMS velocities for layer 2A ranged from 2.24 to 2.65 km s^{-1} with an average of 2.39 ± 0.17 km s^{-1} for the two eastern along-axis locations. Ray tracing was also

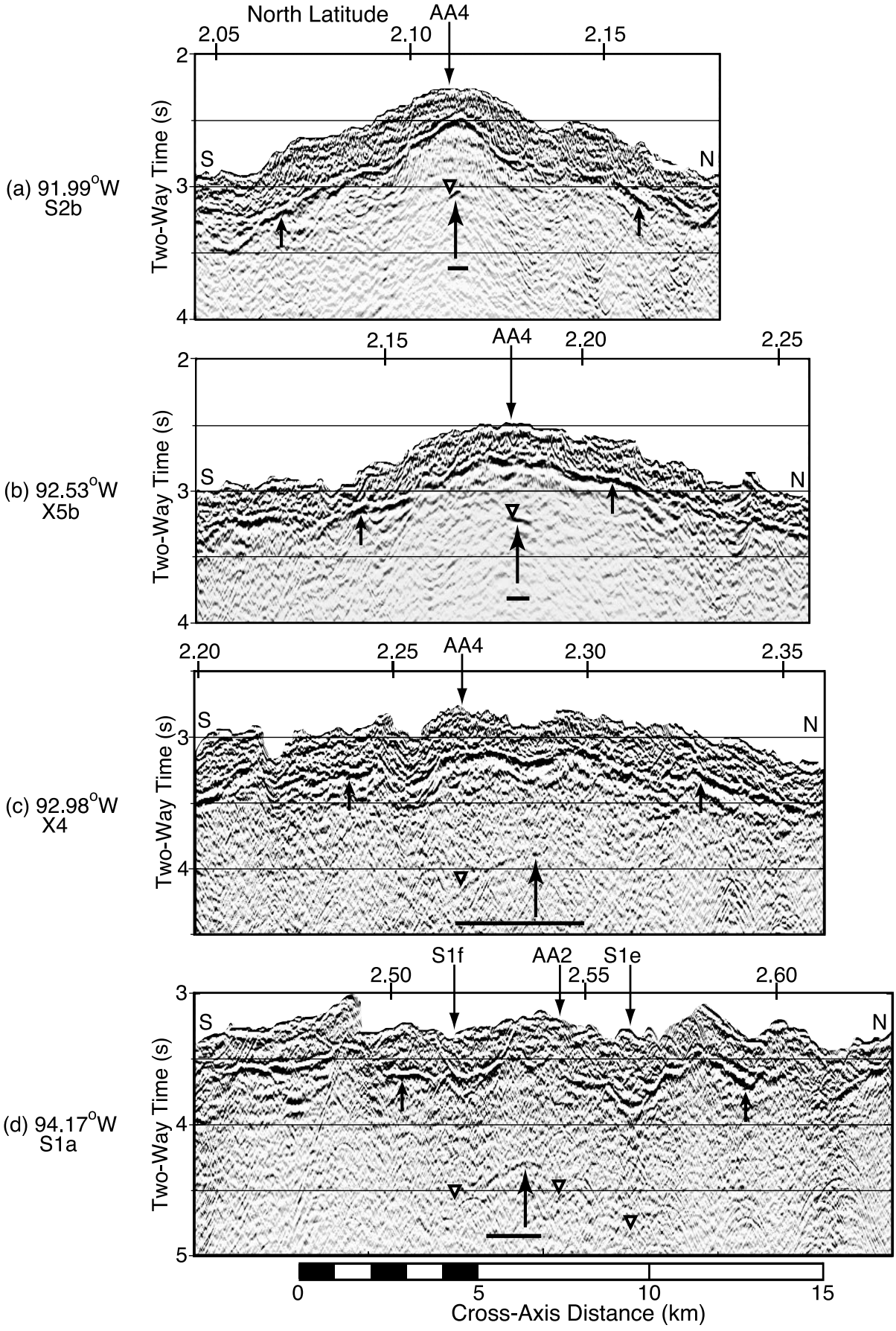
North Latitude
AA4
2.05
2.10
2.15
Two-Way Time (s)
S
N
(a) 91.99°W
S2b
2.15
AA4
2.20
2.25
(b) 92.53°W
X5b
2.20
2.25
AA4
2.30
2.35
(c) 92.98°W
X4
S1f
AA2
S1e
2.50
2.55
2.60
(d) 94.17°W
S1a
0
5
10
15
Cross-Axis Distance (km)

Figure 5

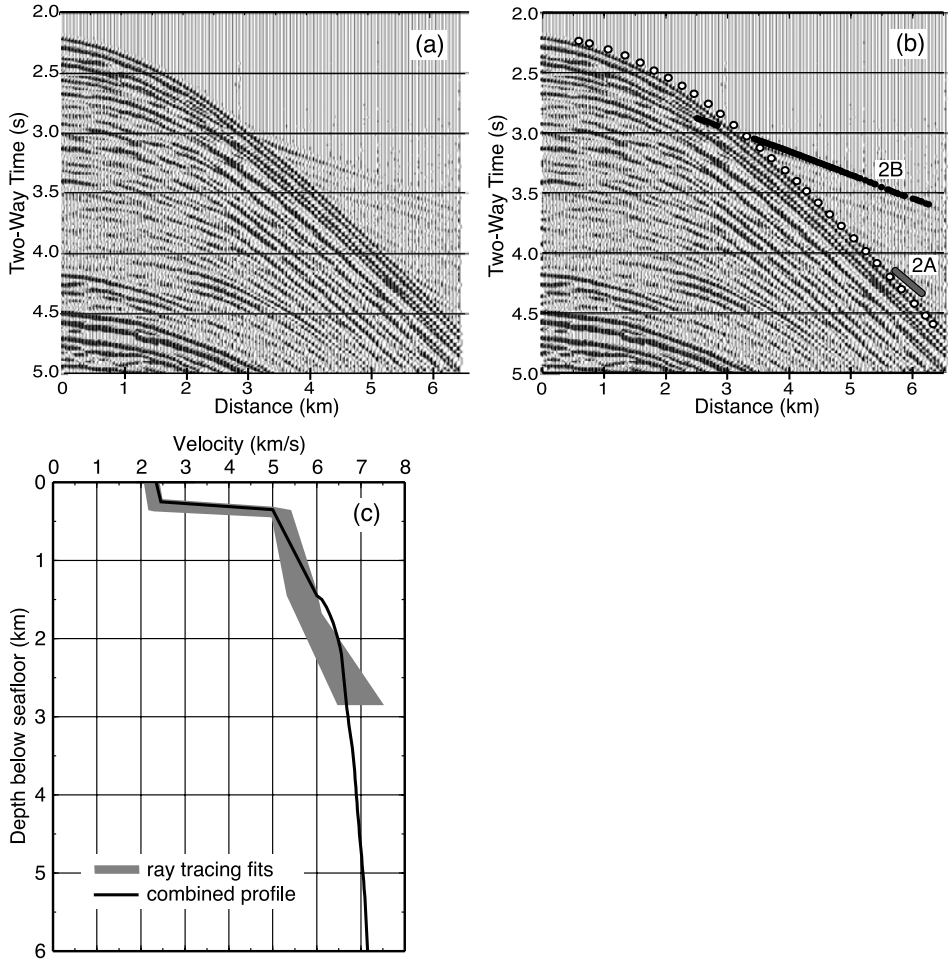

Figure 6. Stacked shot gathers from along-axis survey lines and modeling results of reflections from the uppermost crust. Shot stacks are plotted with a band-pass filter (4–16 Hz) and exponential gain function. Every fourth trace is shown. (a) Stacked shots from 91.47°W. (b) Ray tracing modeling results superimposed on stacked shots. Open circles are fits to picks of the seafloor reflector. Solid circles show the fit to picks of energy turning in the top of layer 2B. Gray bar shows the fit to picks of energy turning in the steep velocity gradient at the base of layer 2A. (c) Velocity profiles. Gray region encompasses ray-tracing fits for 91.47°W and 92.32°W including the velocity profile resulting from the ray tracing fit shown in Figure 6b. Solid line corresponds to velocity profile used for calculation of depth to the top of the axial magma lens. Profile combines results from the wide-angle refraction experiment Gala-3 [*Canales et al.*, 2002] with our ray tracing results from 91.47°W to 92.32°W.

performed for three locations 15–20 km north of the axis: 91.44°W, 92.28°W, and 94.20°W. In these locations, the water depth was too great for picks to be made of rays turning in layer 2A. We were still able to obtain model fits for these areas, but the range of possible fits was greater due to the reduced data set, leading to a greater estimated error of ±0.40 km s^{-1}. Off-axis, the layer 2A RMS velocity varied from 2.49 to 3.08 km s^{-1} with an average of 2.84 ± 0.40 km s^{-1} for all three off-axis locations. Our ray tracing results agree well with *Hussenoeder et al.*'s

Figure 5. Across-axis stacks at various distances along the GSC. Processing is given in Table 1. Along-axis MCS lines cross these profiles at downward pointing arrows and image the magma lens at the lower tips of the inverted open triangles. The axial magma lens reflector is highlighted with large upward pointing arrows. Black bars show the estimated width of the axial magma lens. Small upward pointing arrows indicate the base of layer 2A. (a) Near the hotspot where there is a distinct axial high the axial magma lens is ~0.75 s TWTT below the seafloor. (b) Near the transition from axial high to transitional topography the axial magma lens is still shallow (~0.8 s TWTT below the seafloor) and layer 2A thickens only slightly away from the ridge axis. (c) West of the transition from axial high to transitional topography the magma lens is deeper (~1.0 s TWTT below the seafloor) and off-axis thickening of 2A is more difficult to distinguish. At this location, the magma lens reflector appears to be very wide and slopes to the south. (d) Far from the hotspot the axial magma lens remains deep (~1.1 s TWTT below the seafloor), and we resolve no off-axis thickening of layer 2A.

[2002a] reported extrusive velocities of 2.26 ± 0.08 km s^{-1} on and 2.86 ± 0.20 km s^{-1} 6 km off the axis of the EPR near 17°20′S.

[18] To estimate the thickness of layer 2A along the ridge axis we took the mean RMS velocity from the two eastern on-axis locations and multiplied it by half of the mean two-way time as imaged by the MCS profiles (average of 2A depths in two way travel time over ±200 m from the axis). To estimate the off-axis (>2 km from the ridge axis) thickness of layer 2A we averaged the two-way travel time of layer 2A between 2 and 6–10 km from the axis (depending on the length of the cross-axis MCS line) and then multiplied this average by one half the average near-axis RMS velocity. The average near-axis RMS velocity was calculated as the average of the mean on-axis and mean off-axis RMS velocities for layer 2A to represent the RMS velocity approximately midway between the on-axis and off-axis ray tracing results. Errors for each location along the axis are based on our estimated pick error and the RMS velocity error for on- and off-axis ray tracing model results.

[19] To estimate the depth of the axial magma lens, we combined our ray tracing results for the uppermost crust (top 1.45 km) with the deeper crustal velocity profile obtained from the wide-angle seismic refraction experiments carried out as part of the G-PRIME cruise at 92.0°W (Gala-3) [*Canales et al.*, 2002]. The velocity profile used is shown in Figure 6c. On the basis of the estimated uncertainty in the ray tracing model results, Gala-3 velocity profile reported by *Canales et al.* [2002], and the error of our picks from the MCS profiles, we estimate the average uncertainty in the axial magma chamber depth to be ±110 m.

3. Observations

3.1. Axial Trough

[20] The ridge axis location was determined based on symmetry of the topography to the north and south [*Sinton et al.*, 2003]. We analyzed magnetic data gathered during the G-PRIME and Galapagos 1996 [*Canales et al.*, 1997] cruises and found that the peak of the central axial magnetic anomaly coincided with the axis location picks based on topography after correcting for skewness [*Blacic et al.*, 2002]. Agreement between topographic and magnetic axis locations was excellent east of ∼94.2°W; at a few locations to the west where the zone of active rifting and magmatism is likely to be wider, the magnetic peak is slightly (<2 km) north of the topographic axis location.

[21] The multibeam bathymetry data reveal the development of a trough or small valley along the ridge axis, which we hypothesize to influence the off-axis evolution of layer 2A. Profiles orthogonal to the axis were measured every 0.1° along the axis from the G-PRIME hydrosweep data gridded at 100 m [*Sinton et al.*, 2003]. Examples of the topographic profiles are shown in Figure 2 (bottom). The axial trough depth and width were measured along these profiles as well as along each cross-axis MCS line. Error bars for trough width and depth for each location are estimated based on our minimum and maximum estimates, which primarily depend upon the roughness of the topography. As the axial trough increases in size to the west, it became increasingly difficult to precisely determine the edges of the trough as well as an average depth at a given cross section.

[22] East of ∼92.5°W, the trough is not continuous along the ridge axis, but is present in short segments as noted by *Sinton et al.* [2003]. In this region, the trough may be similar in size and origin to the "axial summit collapse troughs" and "axial summit grabens" recognized along the East Pacific Rise [e.g., *Luyendyk and Macdonald*, 1985; *Gente et al.*, 1986; *Haymon et al.*, 1991, 1997; *Embley et al.*, 1995; *Fornari and Embley*, 1995; *Auzende et al.*, 1996; *Detrick et al.*, 1987, 1993; *Macdonald and Fox*, 1988; *Sinton and Detrick*, 1992; *Fornari et al.*, 1998]. Near ∼92.6°W a larger trough emerges at the axis of spreading with a depth and width of ∼40 km and ∼1.5 m, respectively (Figure 7). From this point to the west, the trough grows in width and depth until reaching a depth of ∼225 m and width of ∼3.5 km near 94.9°W. This feature may share a similar origin to the largest troughs observed along the EPR [*Fornari et al.*, 1998]. West of 95°W, the trough increases rapidly in depth and width reaching ∼300 m in depth and ∼9 km in width by 95.1°W.

3.2. Axial Magma Lens

[23] Near the hot spot, between 91.3° to 92°W, the magma lens can be distinguished ∼0.8 s TWTT below the seafloor as a nearly flat-lying high-amplitude signal in along-axis MCS lines (Figure 4). East of 92°W, the axial magma lens event is high amplitude and can be traced almost continuously to the axial seamount near 91.35°W. From 92°W to 93°W, the reflector is still high amplitude but more discontinuous. Between 93°W and 94°W, the magma lens reflector is even more discontinuous and its amplitude is decreased. All cross-axis lines east of 94.33°W (S1d) image a magma lens (e.g., Figure 5) except line X6 (91.36°W) where a large seamount lies on the ridge axis. We do not see a magma lens reflector in our along- or cross-axis lines west of 94.4°W.

[24] We see a distinct change in the depth of the axial magma lens along the axis from east to west (Figure 8). Near the hot spot, east of ∼92.5°W, the magma lens reflector is ∼0.5–1.0 s TWTT (∼1–2.5 km) below the seafloor. Except where an overlap basin is crossed near 91.6°W, short-wavelength variability in magma lens depth is relatively small (<0.15 s TWTT). Away from this overlap basin, the magma lens depth in this region is similar to that observed along the EPR [*Vera et al.*, 1990; *Kent et al.*, 1993a, 1993b; *Detrick et al.*, 1993; *Mutter et al.*, 1995; *Hooft et al.*, 1997; *Tolstoy et al.*, 1997; *Babcock et al.*, 1998; *Carbotte et al.*, 2000]. Between 92.5°W and 93.0°W the magma lens deepens beneath the ridge axis by ≥50% over an along-axis distance of <45 km. West of ∼92.7°W, the axial magma lens reflector is generally deeper than to the east (1.0–1.5 s TWTT, or 2.5–4.5 km below seafloor), more discontinuous, and shows significant variations in TWTT below the seafloor (0.2–0.3 s TWTT in some locations). The shortest wavelength (∼10–20 km) variability in magma lens depth is slightly greater than the short-wavelength variability east of 92.5°W. In this region, which is relatively far from the Galapagos hot spot, the depth of the axial magma lens is comparable to that along the southern Juan de Fuca Ridge [*Morton et al.*, 1987] and the Valu Fa Ridge of the Lau Basin [*Collier and Sinha*, 1992].

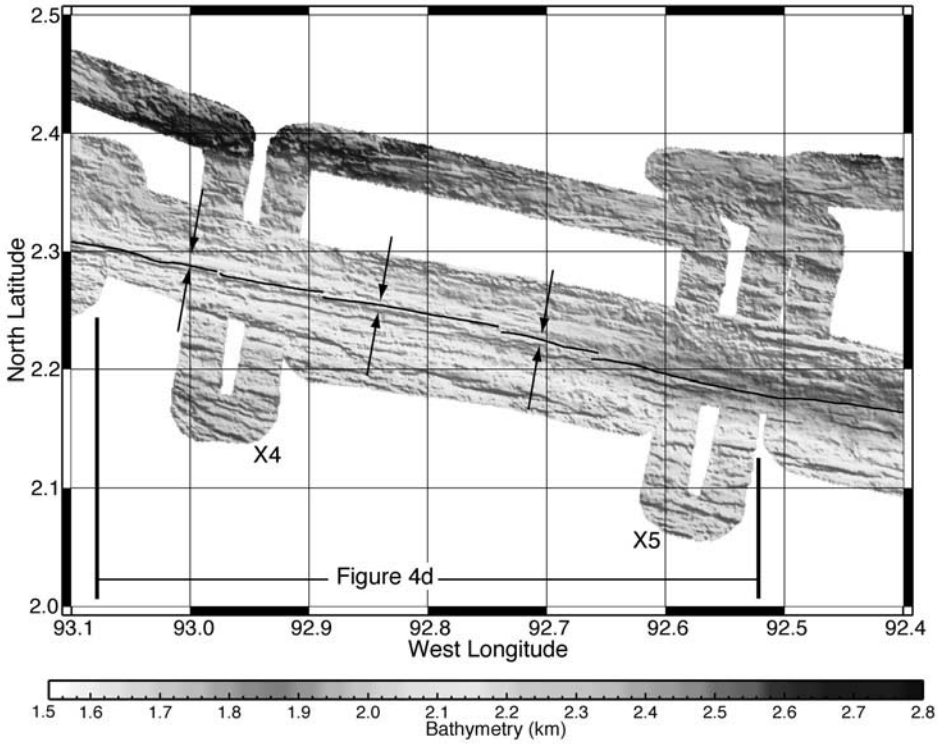

Figure 7. Bathymetry map of GSC showing the region where a prominent axial trough appears and the axial high disappears. Black line marks the location of the ridge axis [*Sinton et al.*, 2003]. Black arrows indicate the approximate bounds of the axial trough. Bold vertical lines indicate extent of line AA4e, Figure 4d. See color version of this figure at back of this issue.

[25] Some of the variability in the TWTT to the magma lens imaged in our survey lines parallel to the ridge axis (Figure 8) may be artifacts of the ship occasionally straying (<2 km) away from the ridge axis (Figure 2). However, an analysis of ship distance from the ridge axis shows no simple correlation with TWTT to magma lens or with the difference between the along-axis picks of magma lens and the minimum TWTT imaged in cross-axis lines. Some of the variability could reflect real changes in the magma lens depth away from the ridge axis. For example, the TWTT of the magma lens imaged in the along-axis line (AA4) near 93.0°W matches the TWTT in the cross-axis image (X4, see Figure 5c and discussion in next paragraph) where the two lines intersect ~1.8 km south of the ridge axis. Regardless, the apparent magma lens depths from the along-axis lines should be interpreted only qualitatively, as revealing the regional trend. We will use the depths imaged in the cross-axis lines in the quantitative analyses below.

[26] The width of the axial magma lens was determined from the migrated cross-axis MCS lines (some examples shown in Figure 5). Prior to migration, the axial magma lens event appeared much broader with an approximately hyperbolic shape. In most cases, migration collapsed these hyperbolae to narrow, linear reflectors. In cross-axis lines S1a at 94.17°W and X4 at 92.98°W (Figure 5), however, the magma lens retained a wide, slightly curved shape even after migration. Increasing the migration velocity in these cases did not result in any further collapse of the magma lens reflector but in overmigration of the edges. The axial magma lens pick locations were converted to distance orthogonal to the axis and the magma lens width was determined as the distance between the northernmost and southernmost picks with an error of ±140 m based on the uncertainty in picking the edges of the magma lens. As suggested by *Kent et al.*'s [1990, 1993b] comparison between migration using stacking velocities and forward modeling of diffractions from the edges of the magma lens, migrated images most likely overpredict the width of the axial magma lens. We therefore consider our magma lens width estimates to be upper bounds.

[27] The width of the axial magma lens also shows significant variation over the study area (Figure 9f). Narrow widths (~0.5 km) appear both close to the hot spot (east of 92°W) where an axial high is present, as well as relatively far from the hot spot (west of ~93.7°W), where axial morphology is transitional. Wider magma lenses are apparent at intermediate distances (92.7–93°W), reaching a maximum value of ~3.5 km near 93.0°W. In general, these widths are comparable to observed magma lens widths along the EPR (~0.3 to ~1.6 km) [*Kent et al.*, 1990, 1993a, 1993b; *Detrick et al.*, 1993; *Perfit et al.*, 1994; *Mutter et al.*, 1995; *Hooft et al.*, 1997; *Carbotte et al.*, 1998, 2000; *Babcock et al.*, 1998], and along the Valu Fa Ridge (0.6 to 2.3 ± 0.4 km) [*Collier and Sinha*, 1992]. It is interesting to note that we find the widest magma lenses just west of the disappearance of the axial high and that a large jump in width occurs between 92.53°W (line X5b) and 92.58°W (line X5a) as the depth of the magma lens increases rapidly coincident with the disappearance of the axial high. However, we do need to keep in mind that the

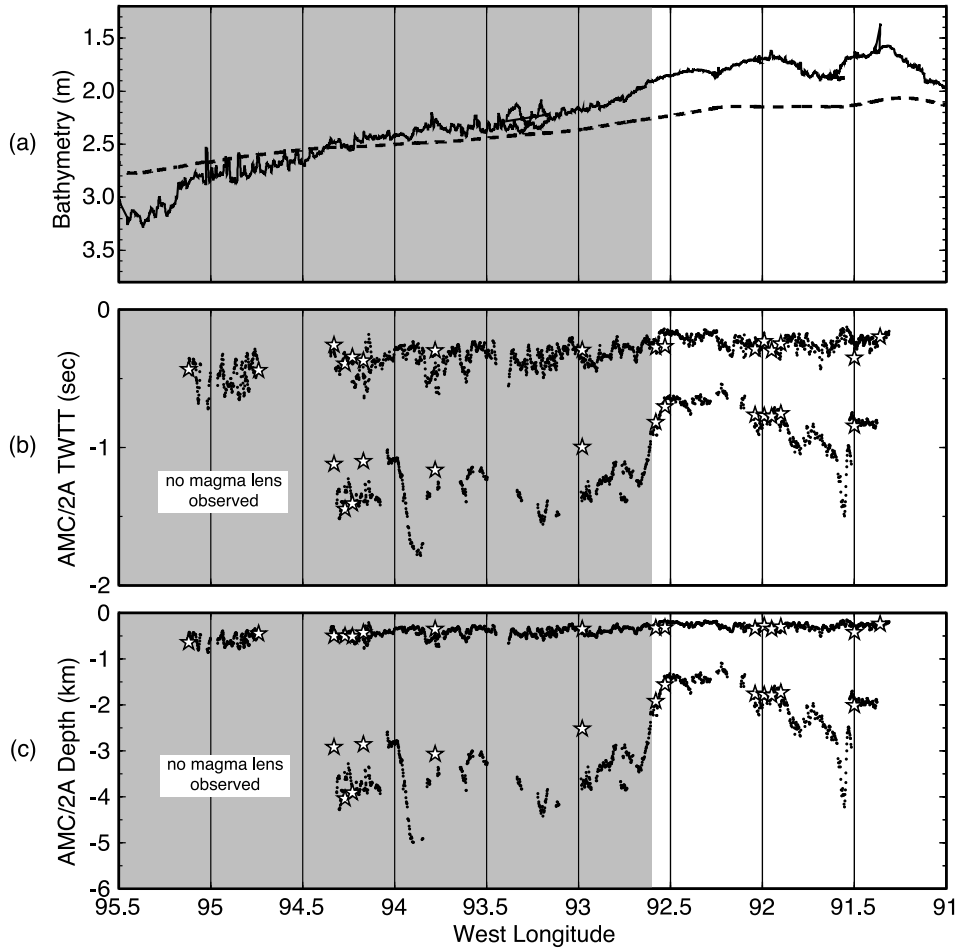

Figure 8. Variation in thickness of layer 2A and depth of axial magma lens along the axis of the western GSC. Shaded area represents region with transitional axial topography, and unshaded area represents region with axial high morphology. The boundary between axial high and transitional topography is placed at 92.6°W, but the disappearance of the axial high occurs over a distance of ~25 km from 92.5° to 92.7°W. (a) Hydrosweep bathymetry along the ridge axis (thin solid line) and filtered bathymetry (dashed line). The difference between the two indicates the height of the local axial topographic high [*Canales et al.*, 2002]. (b) Depth below the seafloor to (top) the base of layer 2A and (bottom) the top of the magma lens in seconds TWTT. Dots are picks from along-axis MCS stacked profiles. Stars are picks at the axis from across-axis MCS stacked and migrated profiles. Uncertainty is ±0.035 s TWTT for the base of layer 2A and ±0.032 s TWTT for the top of the axial magma lens. (c) Depth below the seafloor to (top) the base of layer 2A and (bottom) top of the axial magma lens. Average uncertainties are ±62 m for the base of layer 2A and ±110 m for the top of the axial magma lens.

increased width of the magma lens could be a transient feature resulting from recent or impending injections of melt or eruptions. Thus unlike magma lens depth, magma lens width does not display a simple correlation with distance from the hot spot and axial morphology. This large variability in magma lens width suggests that the zone of dike intrusion could be variable both in space and time, offering an opportunity to test this effect on the structure of seismic layer 2A.

3.3. Layer 2A

[28] The on-axis thickness of layer 2A shows both long- and short-wavelength variation over the length of the study area along the axis (Figures 8b and 8c). Near the hot spot, east of 92.5°W, layer 2A is relatively thin (0.2–0.35 s TWTT or 0.24–0.42 km), with relatively small amplitude short-wavelength (<10 km) variability. West of 92.7°W the thickness of layer 2A is greater and more variable (~0.3–0.5 s TWTT or ~0.36–0.60 km) than to the east. In this region, the layer 2A interface appears faulted in some locations and even disappears over a few short intervals. It is likely that faulting contributes to short-wavelength variations in thickness, which can be as large as 0.4 s TWTT (~500 m) in some locations. The transition from thin to thick 2A coincides with the increase in depth of the axial magma lens, the appearance of the axial trough, and the disappearance of the axial topographic high between 92.5°W and 92.7°W (Figure 7). The link between thickness of layer 2A and depth to the magma lens is examined in section 4.

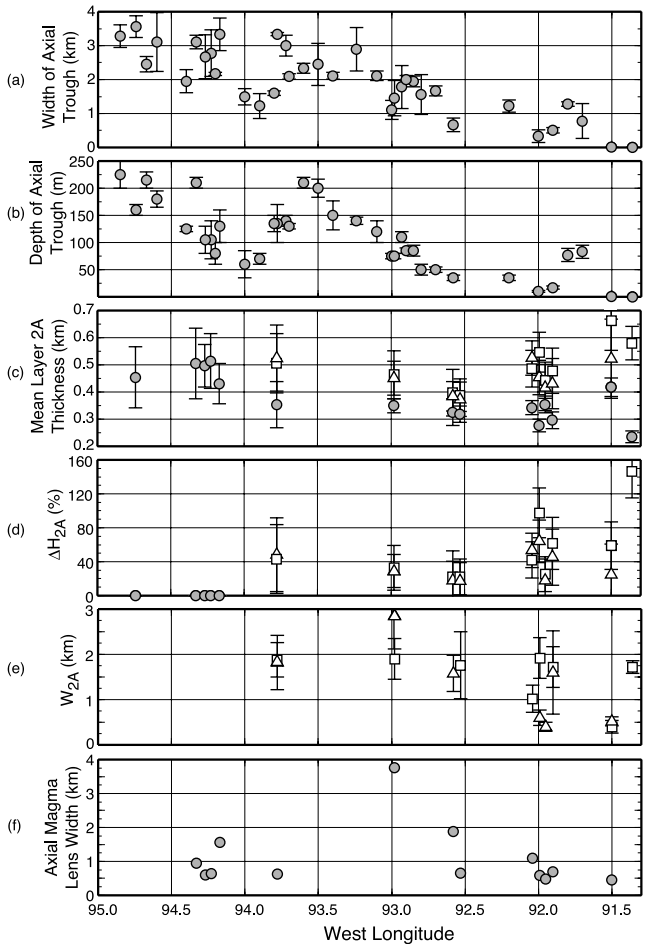

Figure 9. Along-axis variations in ridge properties observed in MCS across-axis profiles and in the bathymetry data. (a) Width of the axial trough. Error bars are shown for areas with estimated error greater than the size of the plotted circle. Error estimates are based on map grid spacing and uncertainty in picking trough dimensions. (b) Depth of the axial trough. Errors are shown as in Figure 9a. (c) Mean layer 2A thickness. Triangles and squares represent mean off-axis layer 2A thickness to the north and south of the axis, respectively. Gray circles represent mean on-axis thickness of layer 2A for across-axis lines east of 94°W and mean layer 2A thickness for the entire across-axis line west of 94°W, where no off-axis thickening occurs. (d) Amplitude of off-axis thickening of layer 2A, ΔH_{2A}, in percent of the on-axis layer 2A thickness. Triangles represent amplitude north of the axis, and squares represent amplitude south of the axis. Where off-axis thickening was not observed (west of 94°W) thickening amplitude was set to zero. (e) Width of off-axis thickening of layer 2A, W_{2A}. Triangles represent width to the north of the axis and squares represent width to the south of the axis. Error estimates were determined by performing a Gaussian fit to the layer 2A picks including the pick error of ±0.035 s TWTT. (f) Magma lens widths determined from migrated cross-axis profiles. Uncertainty is ±140 m.

[29] The width and degree to which seismic layer 2A thickens away from the ridge axis were estimated from our cross-axis lines (e.g., Figure 5). The zero age thickness of layer 2A was determined from picks of the base of layer 2A taken from the time migrated cross-axis seismic profiles. Picks within 0.2 km of the axis were used to calculate the average on-axis thickness except at 93.78°W (X3) where picks within 1.0 km of the axis were used because a topographic peak at the axis obscured the underlying image of the base of layer 2A. The average off-axis thickness is based on picks on both sides of the ridge axis >2 km from the axis. Exceptions are at 91.50°W (X7) and 91.99°W (S2b) where layer 2A thickens more rapidly with off-axis distance, allowing us to use picks $\geq$1.0 km and $\geq$1.5 km from the axis, respectively, to calculate the average. We determined the magnitude of the off-axis thickening by taking the difference between the average on-axis and average off-axis thickness of layer 2A for cross-axis profiles where off-axis thickening was clearly observed (east of 94°W).

[30] Average on- and off-axis thicknesses of layer 2A are plotted along the axis in Figure 9c with errors based on the standard deviation of the TWTT picks and RMS velocity error. The magnitude of thickening is presented as a percent of the on-axis thickness ΔH_{2A} (Figure 9d); ΔH_{2A} = 10% means that the off-axis thickness of layer 2A is 10% thicker than the on-axis thickness. We clearly see off-axis thickening east of 94°W with the highest magnitudes of thickening east of 92.5°W (see also Figure 5a). A dramatic (EPR-like) doubling in thickness (>100% ΔH_{2A}) occurs to the south of the axis at 91.36°W (line X6), however a seamount on the northern slope of the ridge prevents a determination of ΔH_{2A} on the north side of the ridge axis. The magnitude of thickening decreases away from the hot spot to the west, reaching a local minimum in ΔH_{2A} between 92.5° and 92.6°W (X5a, X5b, see Figure 5b) right where the axial trough appears in the bathymetry data (Figure 7). Nearer to the hot spot where ΔH_{2A} is large, we also see larger asymmetries in ΔH_{2A} about the ridge axis, however, there is no preferential thickening on one side compared to the other (outside our error estimates). Thus the presence of the hot spot to the south of the GSC does not appear to systematically affect the evolution of layer 2A on the south side of the axis any differently than on the north side of the axis. West of 94°W, we are unable to identify any off axis thickening. If any such thickening occurs in this region, it is smaller than the relatively large variability in 2A thickness, which may be associated with faulting.

[31] To characterize the cross-axis width over which layer 2A thickening occurs, we fit a Gaussian curve to the picks of the base of layer 2A on each side of each cross-axis profile. Examples of the Gaussian fit to the base of layer 2A are shown in Figure 10. In a few locations it was not possible to obtain a meaningful Gaussian fit both north and south of the axis and in these cases the profiles only have estimates from one side of the axis. We define the characteristic width W_{2A} as twice the standard deviation of the Gaussian fit. The lowest values of W_{2A} (<0.5 km) occur east of ~92°W and the highest values (>1.5 km) occur to the west (Figure 9e). These observations indicate a weak trend of increasing W_{2A} to the west. Asymmetry across

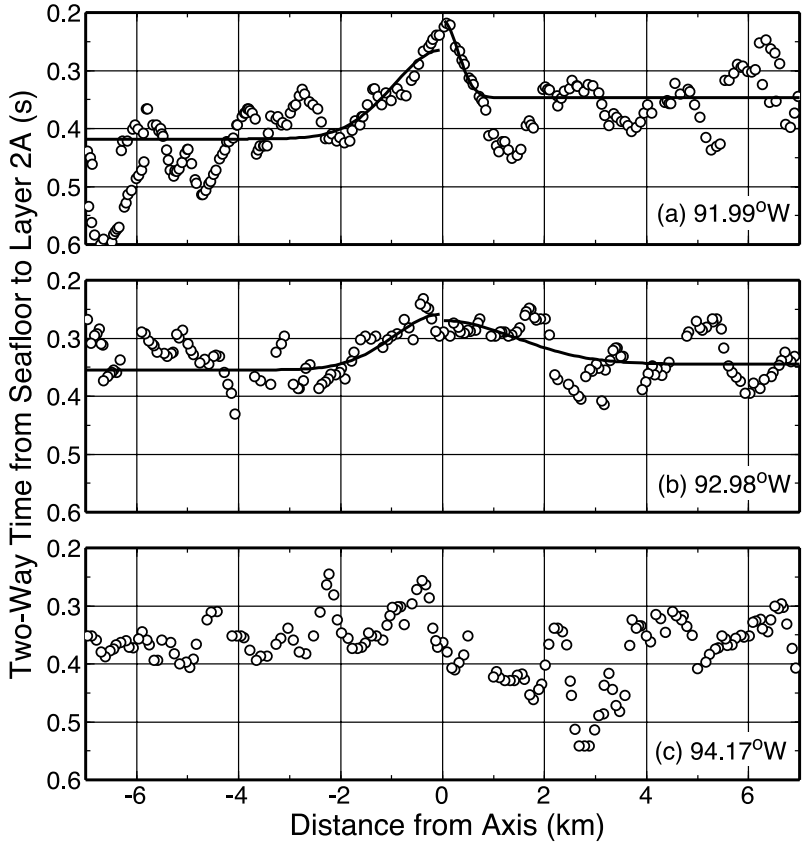

Figure 10. Thickness of layer 2A across the axis at three locations: (a) 91.99°W, line S2b, (b) 92.98°W, line X4, and (c) 94.17°W, line S1a. Open circles are picks of the base of layer 2A obtained from time migrated cross-axis MCS profiles. Solid lines are Gaussian fits to the near-axis picks for determination of the width of off-axis thickening of layer 2A. The fits were constrained by the mean off-axis layer 2A thickness but were unconstrained at the axis in order to obtain the best fit to the shape of layer 2A. Each side of the axis was fit separately. No off-axis thickening was observed at 94.17°W (S1a).

the axis is variable again suggesting that the evolution of layer 2A on the south side of the axis is not affected more strongly than on the north side of the axis by the presence of the hot spot.

3.4. Variations With Distance From the Hot Spot

[32] The major characteristics of on-axis layer 2A thickness, magma lens depth, axial morphology, and percent of off-axis 2A thickening ΔH_{2A}, as summarized in Figures 8 and 9, differ east and west of ~92.5°W. East of 92.5°W and near to the hot spot, the axial magma lens is relatively shallow and narrow. Layer 2A is relatively thin at the ridge axis and thickens off axis with a wide range in both the magnitude (ΔH_{2A}) and width (W_{2A}) of off-axis thickening. This region is contained within the Eastern Province of the western GSC as defined by *Sinton et al.* [2003], characterized by a prominent axial high that is occasionally and locally cut by a narrow trough. West of 92.5°W, the axial magma lens, on average, is ≥50% deeper than east of 92.5°W, though average magma lens width is similar between the two regions. On axis, layer 2A thickens to the west. Off-axis thickening of layer 2A is observed as far west as ~93.8°W. Where thickening is observed, ΔH_{2A} is less and W_{2A} is greater than east of 92.5°W. The region west of 92.5°W is contained within *Sinton et al.*'s [2003] Middle Province, characterized by topography that is intermediate between an axial high and a rift valley. In the Middle Province, the axis lies within a prominent axial trough that widens and deepens to the west.

4. Discussion: Correlations and Implications for Controls on Eruption Processes

[33] In this section we discuss correlations between topographic characteristics and layer 2A and axial magma lens geometry using the cross-axis MCS images as the source of information for layer 2A and the axial magma lens.

4.1. On-Axis Layer 2A Thickness and Depth to Axial Magma Lens

[34] We document a strong positive correlation between the on-axis thickness of layer 2A and the depth of the magma lens (Figure 11). This correlation supports a model that invokes a balance between the pressure on the magma lens and the pressure required to push magma up a dike to the surface [*Buck et al.*, 1997]. In the simplest case, magma lens pressure is the weight of the overlying rocks and the pressure required to feed magma to the surface is the weight of the magma. In this case, a linear relation between

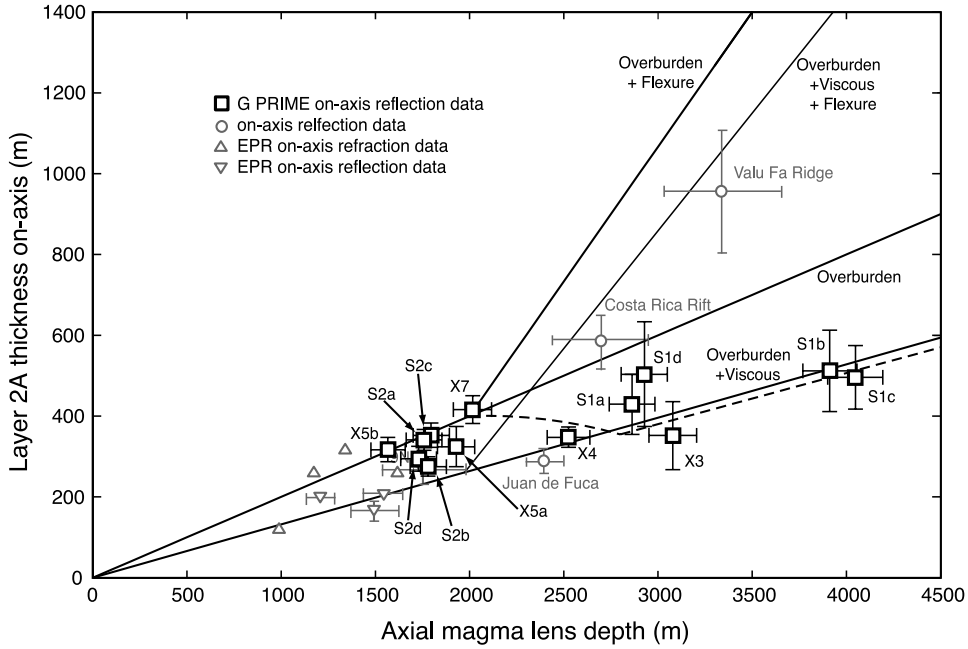

Figure 11. Depth to the axial magma lens plotted against on-axis thickness of layer 2A [after *Buck et al.*, 1997]. Triangles and inverted triangles represent locations along the East Pacific Rise (full spreading rate from ~85 to ~150 mm yr^{-1} [*Klitgord and Mammerickx*, 1982; *DeMets et al.*, 1990, 1994; *Harding et al.*, 1993; *Mutter et al.*, 1995]). Circles represent intermediate rate spreading ridges (full spreading rates are 59.6 mm yr^{-1} for Juan de Fuca Ridge [*Purdy et al.*, 1992], 30–38 mm yr^{-1} for Costa Rica Rift [*Klitgord et al.*, 1975; *Hey et al.*, 1977] and 60 mm yr^{-1} for Valu Fa Ridge [*Purdy et al.*, 1992]). Heavy squares are data from across-axis MCS survey lines conducted on the G-PRIME cruise. Solid lines represent results of model calculations of *Buck et al.* [1997]. For overburden alone, lava density is 2150 kg m^{-3}, intrusive basalt density is 2900 kg m^{-3}, magma density is 2750 kg m^{-3}, and the dynamic pressure gradient is zero. "Overburden plus viscous" includes a dynamic pressure gradient of 500 Pa m^{-1}. "Overburden plus flexure" includes an increase in magma pressure due to the extra weight of the regionally compensated topography. Dashed line shows results of including a linear increase in magma density of 55 kg m^{-3} between magma lens depths 2000 and 2800 m without any viscous or flexure effects included.

extrusive layer thickness and magma lens depth is predicted with a slope of

$$R = (\rho_i - \rho_m)/(\rho_i - \rho_e), \quad (1)$$

where ρ_i, ρ_m, and ρ_e are the densities of the dikes, the magma, and the extrusives, respectively. One complication is viscous pressure loss due to magma flow through the dike. This effect is predicted to reduce the height that magma can rise and thus reduce the thickness of the extrusive layer for a given magma lens depth. Finally, flexure of the axial lithosphere can put the ridge axis in regional isostatic compensation. Compared to the situation of local isostasy, which is assumed in (1), regional compensation can increase the overburden pressure on the magma lens and allow for the construction of a thicker layer 2A (Figure 11).

[35] In the eastern region of our study area (east of 92.5°W) where the magma lens is shallow, the ratio R of layer 2A thickness to magma lens depth is most consistent with the simplest effect of just overburden and magma weight (1), with ρ_i = 2900 kg m^{-3}, ρ_m = 2750 kg m^{-3}, and ρ_e = 2150 kg m^{-3} (Figure 11). There is no need to invoke viscous reduction of magma pressure head or flexural effects in this region. In the western region (west of 92.5°W) where the magma lens is deeper, the ratio R is, on average, less than that predicted for overburden pressure alone. This contrasts with the results of the other intermediate spreading ridge segments (Costa Rica Rift and Valu Fa Ridges) discussed by *Buck et al.* [1997], which have larger ratio R.

[36] One possible cause for the reduction in R in the western part of our study area is that viscous pressure loss is more important than to the east. The decrease in the vertical pressure gradient due to viscous magma flow γ depends on magma viscosity μ, average speed of magma flow through the dike U and the characteristic dimension D of the dike or magma conduit according to [e.g., *Turcotte and Schubert*, 1982, p. 238]

$$\gamma \sim \mu U D^{-2}. \quad (2)$$

An increase in γ to the west caused by an increase in magma viscosity is unlikely given the nearly uniform viscosity estimates based on composition, crystallization temperature, and crystallinity of the lavas dredged along the ridge axis between ~91°W and ~98°W [*Behn et al.*, 2004]. It is also difficult to invoke an increase in magma flow rate

to the west given the westward increase in the frequency of axial seamounts from 92.5°W to 95.5°W, which is more consistent with less effusive volcanic events to the west [*Behn et al.*, 2004] (though we know that the frequency and size of seamounts changes very little east of 92.5°W). If viscous pressure loss is an important factor in reducing R to the west, then this implies a decrease in the average size of magma conduits (D). Indeed, the high sensitivity of γ on D would allow relatively small reductions in D to the west to cause important increases in γ.

[37] Alternatively, the reduced ratio R could result from an increase in magma density to the west without any viscous pressure loss (see equation (1)). We obtain an improved fit to our data (dashed line in Figure 11) by plotting a line with a linear increase in magma density ρ_m from 2750 to 2805 kg m^{-3} between magma lens depths of 2000 and 2800 m, respectively, and keeping ρ_m = 2805 kg m^{-3} for magma lens depths >2800 m. Analyses of lava samples collected during the G-PRIME experiment provide some constraints. From east of 92.5°W to the west, mean values of Mg # (atomic MgO/(MgO + FeO)), computed liquidus temperature, and crystallinity increase, whereas mean water content decreases [*Detrick et al.*, 2002; *Behn et al.*, 2004; *Cushman et al.*, 2004]. An increase in magma density to the west is consistent with an increase in crystallinity and decrease in water content, but it requires that these effects on density dominate over the effects of increasing Mg # and magma liquidus temperature. What may be more important is vesicularity. As the vesicularity of lava tends to decrease with decreasing volatile contents and increasing magma pressure, the less volatile-rich magma arising from the deep magma chamber to the west of 92.5° is likely to be, on average, less vesicular and more dense [*Behn et al.*, 2004] as it rises to build the extrusive layer.

[38] The model proposed by *Buck et al.* [1997] helps to explain the correlation between on-axis layer 2A thickness and depth to the axial magma lens, but it does not explain why both magma lens depth and layer 2A thickness increase abruptly near 92.5°W, coinciding with the disappearance of the distinct axial high. The rapid transition from axial high to transitional topography supports the concept of a "threshold" mechanism proposed by *Phipps Morgan and Chen* [1993] and *Chen and Lin* [2004]. In this model, axial morphology is controlled by the thermal structure at the ridge axis which is mainly influenced by magma supply and hydrothermal circulation. They note the existence of a threshold crustal thickness at a given spreading rate about which small changes in crustal thickness lead to large changes in thermal structure and therefore the depth at which the crust is hot enough to maintain a magma lens. They also note that variations in axial thermal structure are most sensitive at intermediate spreading rates (half rates of 20–30 mm yr^{-1}) to small changes in magma supply. Along the intermediate spreading western GSC, magma supply apparently changes enough to cross the threshold from axial high to transitional topography at crustal thicknesses of ~6.8 km [*Canales et al.*, 2002] and crustal production rates of ~0.35–0.36 × 10^6 m^3 km^{-1} yr^{-1} [*Sinton et al.*, 2003]. This transition coincides with a deepening of the axial magma lens and a corresponding increase in the on-axis thickness of layer 2A. Hence the shallow structure of the mid-ocean ridge crust is linked to the properties of the mantle through its effect on magma supply and the heat budget of the entire crust.

4.2. Off-Axis Thickening of Layer 2A

[39] Results of stochastic modeling by *Hooft et al.* [1996] provide quantitative predictions of the geometry of off-axis thickening of layer 2A. In their model, the key variables controlling width and magnitude of thickening are the characteristic lava flow length, σ_e, and the characteristic intrusion zone width, σ_i (axial zone within which diking occurs and eruptions can emerge). Their models predict the extrusive layer to thicken off axis if individual lava flows extend outside of the zone of intrusion (i.e., $\sigma_e > \sigma_i$). For constant σ_e, they predict wider intrusion zones σ_i to cause layer 2A to thicken over a greater distance (i.e., larger W_{2A}) but by a smaller magnitude (i.e., smaller ΔH_{2A}) For constant σ_i, they predict longer lava flows (greater σ_e) to lead to greater widths W_{2A} and magnitudes ΔH_{2A} of thickening. These predictions provide a general framework within which to analyze and interpret our data. Here we assume that the intrusion zone width is proportional to the width of the magma lens. Furthermore, the flow length may be linked to the width of the axial trough; σ_e may increase with increasing axial trough width, provided the trough is deep enough to limit the length of lava flows.

[40] The width of the axial magma lens (intrusion zone width, σ_i) is plotted against ΔH_{2A} and W_{2A} in Figures 12a and 12b. For narrow magma lenses our observations show large variability with ΔH_{2A} spanning 0–100% and W_{2A} spanning 0.3–2.0 km. For magma lenses greater than ~1 km wide, ΔH_{2A} and W_{2A} are more limited in variability with ΔH_{2A} limited to values ≤60% and $W_{2A} \geq$ 1.0 km. These trends are consistent with *Hooft et al.*'s [1996] predicted effects of increasing σ_i with constant σ_e. In Figures 12c and 12d, axial trough width is plotted against ΔH_{2A} and W_{2A}. For trough widths <0.8 km we see large variability, with ΔH_{2A} spanning 15–100% and W_{2A} spanning 0.3–2.0 km. For troughs wider than ~0.8 km, we see smaller variability in both quantities, with ΔH_{2A} increasing slightly with trough width to a maximum of ~50% (i.e., for locations east of ~94°W off-axis where thickening occurs) and W_{2A} showing no systematic change but remaining ≥1.8 km.

[41] The correlation or lack of correlation between layer 2A geometry and the factors that can influence the accumulation of extrusive crust can help us identify the most important processes at work. We see evidence that magma lens width can influence layer 2A thickening in a manner consistent with *Hooft et al.* [1996], but we do not see such clear evidence for a predictable effect due to axial trough width. Also, an unpredicted large variability in both ΔH_{2A} and W_{2A} occurs where both the magma lens and axial trough are most narrow. Finally, we see no apparent thickening of layer 2A west of ~94°W even though the axial trough is wider than the magma lens (i.e., $\sigma_e > \sigma_i$) which implies that off-axis thickening is possible [*Hooft et al.*, 1996]. These complications suggest that factors other than the axial trough could be important in limiting the off-axis extent of lava flows (σ_e).

[42] One possibility, as noted by *Mutter et al.* [1995] and *Carbotte et al.* [1998], is that magma supply limits the off-axis extent to which lava can flow. Another factor may be the slope of the axial topographic high. East of 92.5°W, the

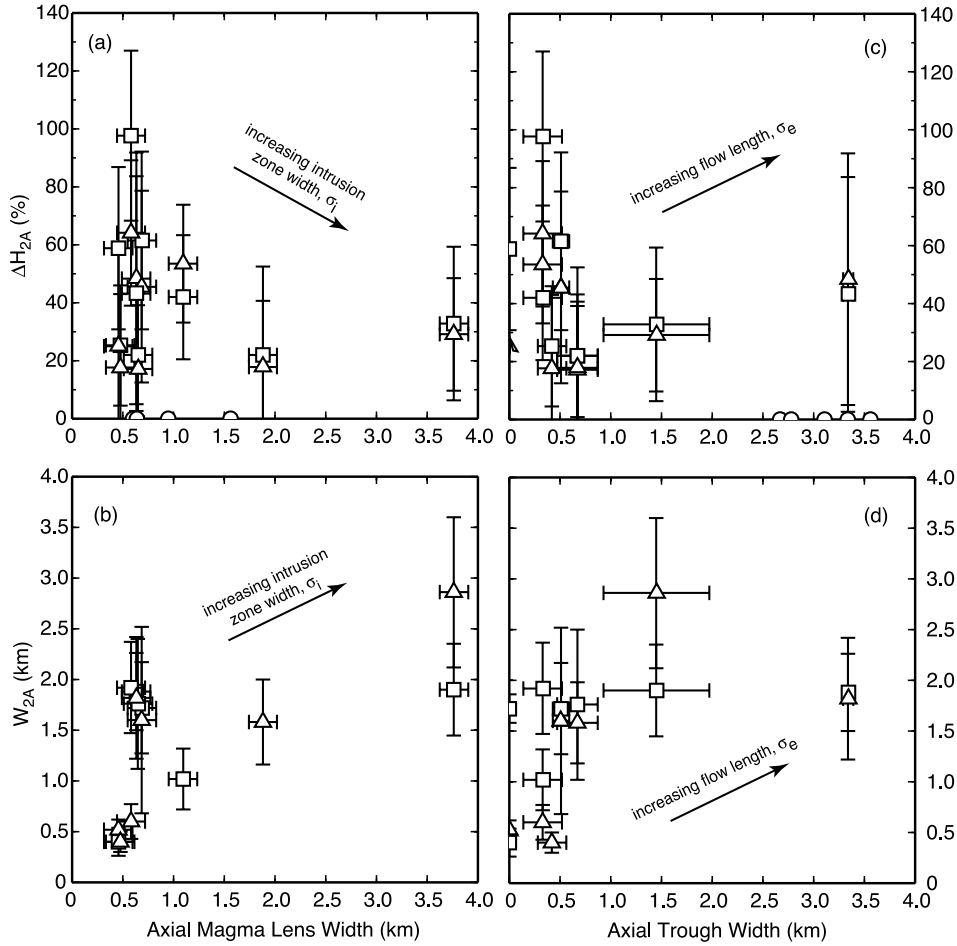

Figure 12. (a) Amplitude of off-axis thickening of layer 2A, ΔH_{2A}, and (b) width of off-axis layer 2A thickening, W_{2A} plotted against the axial magma lens width. Increasing magma lens width correlates with increasing W_{2A}. (c) ΔH_{2A} and (d) W_{2A} plotted against the axial trough width. All points except circles in Figures 12a and 12c are east of 94°W where off-axis thickening of layer 2A is observed. Arrows schematically show predicted effects of shown variables by *Hooft et al.* [1996].

prominence of sheet flows collected during the G-PRIME sampling program suggests more effusive and more voluminous eruptions [*Behn et al.*, 2004]. Voluminous eruptions can overflow small axial troughs and flow substantially off axis down the slope of the axial topographic high. These factors may explain the wide range of amplitudes and widths of off axis layer 2A thickening, largely independent of the narrow axial trough. West of ~94°W, the axial high is absent, faulting dominates the topography, and the dominance of pillow lavas suggests lower average effusion rates [*Behn et al.*, 2004]. These factors most likely limit σ_e to be $<\sigma_i$ and thus minimize any off axis thickening of layer 2A.

[43] The lack of off-axis thickening west of 94°W could also be related to recent changes in the location of the neovolcanic zone. Interpretation of bathymetry in the region between 94° and 94.4°W suggests two small southward offsets in the ridge segmentation: one at ~94.2°W and the other at ~94.3°W (Figure 2). The central magnetic anomaly peak, however, lies ~1.5–2 km to the north of the axis. We also see axial magma lens reflections at about the same depth in all three axis parallel lines (AA2, S1f, S1e) in this region. If the ridge axis has shifted south in the last ~100 kyr it could result in a time-averaged intrusion zone width σ_i that exceeds the length of individual lava flows σ_e and thus prevent any off-axis thickening of the layer 2A.

[44] Finally, we note that our observation of no off-axis thickening of the extrusive crust west of 94°W depends upon our assumption that it encompasses both the shallow low-velocity layer and the deeper velocity gradient within layer 2A. *Hussenoeder et al.* [2002b] used waveform inversions of MCS data from the slow spreading MAR to show that the shallow, low-velocity layer thickens away from the inner valley axis of the MAR but that the transition from low to high velocities in the lower part of layer 2A thins off axis. The combination of the two changes results in a lack of off-axis increase in the total layer 2A thickness at the MAR much as we observe at the GSC west of 94°W. However, *Hussenoeder et al.* [2002a, 2002b] attribute the thickening of the shallow, low-velocity layer at the MAR to an off-axis thickening of the extrusive crust. It is possible that such thickening occurs within layer 2A along the GSC west of 94°W, but the present analyses are insufficient to constrain such detailed structure. Regardless, it is clear that

the extrusive crust along the GSC west of 94°W evolves quite differently than it does to the east.

5. Conclusions

[45] We have examined multichannel seismic and bathymetry data from a portion of the western GSC to examine the relationships between seismic layer 2A, axial magma lens, and axial morphology. Where there is an axial high, east of ~92.5°W, both the top of the magma lens and the base of layer 2A are relatively shallow. West of 92.5°W, axial morphology is transitional between an axial high and an axial valley and both the base of layer 2A, and the magma lens are significantly deeper. The changes in layer 2A thickness that we observe both along and across the axis are most easily interpreted in terms of layer 2A coinciding with the extrusive volcanic crust. The westward increase in on-axis layer 2A thickness with increasing magma lens depth supports the model of *Buck et al.* [1997], which invokes a balance between the pressure on the magma lens and pressure required to feed magma to the surface and build the extrusive layer. The decrease in the ratio of on-axis layer 2A thickness to depth of the axial magma lens west of 92.5°W–92.7°W could be the result of one or a combination of two factors: an increase in viscous head loss due to reduction in the characteristic size of magma conduits or an increase in magma density due to a decrease in water content and vesicularity, and increase in crystallinity. West of ~94.4°W we do not see a clear axial magma lens.

[46] The Galapagos Spreading Center shows off-axis thickening of layer 2A, but only over that portion of our study area most influenced by the Galapagos hot spot (~94° to ~91.3°W). East of 92.5°W the ridge is most proximal to the Galapagos hot spot, has a prominent axial high morphology, and the magma lens is generally narrow. In this region the magnitude ΔH_{2A} and cross-axis width W_{2A} of off-axis thickening of layer 2A is highly variable, with ΔH_{2A} extending from near zero to ~150% and W_{2A} extending from <0.5 to 1.9 km. Between 92.5°W and ~94°W, where there is transitional axial topography, the magma lens is wide and seismic layer 2A thickens off axis by a small magnitude ($\Delta H_{2A} < 45\%$) over intermediate widths ($W_{2A} \geq 1.5$ km). Correlations between magma lens width and ΔH_{2A} and W_{2A} support the notion that narrow magma lenses tend to focus melt delivery to the ridge axis and allow for lava to flow outside of the neovolcanic zone and substantially thicken the extrusive layer (i.e., large ΔH_{2A}) relatively close to the ridge axis (i.e., small W_{2A}). Correlations between ΔH_{2A} and W_{2A} and the width of the axial trough are unclear or are inconsistent, and we do not see off-axis thickening of layer 2A west of ~94°W where we might expect to see thickening since the magma lens is narrower than the axial trough (if the axial trough is a limiting factor to lava flow length). The last two results suggest that factors such as the lack of a sloping axial high and limited magma supply are more important in limiting the off-axis extent of lava flows. Short-term changes in the location of the axial neovolcanic zone may also promote the development of a more uniform extrusive layer thickness. The along-axis variation in magma supply (reflected by the westward decrease in crustal thickness from ~8 to ~6 km reported by *Canales et al.* [2002]) imposed by the Galapagos hot spot probably most directly influences the crustal heat budget; the crustal heat budget controls the axial morphology and magma lens depth, which in turn, influence the pattern of lava eruptions. In this way, the Galapagos hot spot indirectly influences the eruptive processes that construct the shallow crust of the western GSC.

[47] **Acknowledgments.** We would like to thank the captain and crew of the R/V *Maurice Ewing* plus all the scientists who took part in cruise EW0004. We also extend thanks to the Ecuadorian government and to the Ecuadorian observers for allowing us to conduct research in their waters. Paul Henkart, G. Kent, A. Harding, and B. Zelt have our thanks for providing the various plotting and computational packages used in this project. We would also like to thank S. Bazin, E. Hooft, D. Scheirer, and our anonymous Associate Editor for their valuable comments and suggestions during the review process. This project was funded by NSF-OCE-0002189. This is SOEST contribution 6432.

References

Anderson, R. N., et al. (1982), DSDP Hole 504B, the first reference section over 1 km through Layer 2 of the oceanic crust, *Nature*, *300*, 589–594.

Auzende, J. M., et al. (1996), Recent tectonic, magnetic and hydrothermal activity on the East Pacific Rise between 17° and 19°S: Submersible observations, *J. Geophys. Res.*, *101*, 17,005–18,010.

Babcock, J. M., A. J. Harding, G. M. Kent, and J. A. Orcutt (1998), An examination of along-axis variation of magma chamber width and crustal structure on the East Pacific Rise between 13°30′N and 12°20′N, *J. Geophys. Res.*, *103*, 30,451–30,467.

Baran, J. M., J. R. Cochran, S. Carbotte, and M. Nedimovic (2003), Upper crustal variations due to mantle temperature variations along the Southeast Indian Ridge, *Eos Trans. AGU*, *84*(46), Fall Meeting Suppl., Abstract T12D-0502.

Bazin, S., et al. (2001), Three-dimensional shallow crustal emplacement at the 9°03′N overlapping spreading center on the East Pacific Rise: Correlations between magnetization and tomographic images, *J. Geophys. Res.*, *106*, 16,101–16,117.

Becker, K., et al. (1989), Drilling deep into young oceanic crust, Hole 504B, Costa Rica Rift, *Rev. Geophys.*, *27*, 79–101.

Behn, M. D., J. M. Sinton, and R. S. Detrick (2004), Effect of the Galapagos hotspot on seafloor volcanism along the Galapagos Spreading Center (90.9–97.6°W), *Earth Planet. Sci. Lett.*, *217*, 331–347.

Blacic, T. M., G. Ito, R. Detrick, J. P. Canales, and J. Sinton (2002), Shallow crustal structure along the western Galapagos Spreading Center 91.3° to 95.2°W: Correlations between axial magma lens, layer 2A and topographic characteristics, *Eos Trans. AGU*, *83*(47), Fall Meet. Suppl., Abstract T72C-01.

Buck, W. R., S. M. Carbotte, and C. Mutter (1997), Controls on extrusion at mid-ocean ridges, *Geology*, *25*(10), 935–938.

Burnett, M. S., D. W. Caress, and J. A. Orcutt (1989), Tomographic image of the magma chamber at 12°50′N on the East Pacific Rise, *Nature*, *339*, 206–208.

Canales, J. P., J. J. Danobeitia, R. S. Detrick, E. E. E. Hooft, R. Bartolome, and D. F. Naar (1997), Variations in axial morphology along the Galapagos Spreading Center and the influence of the Galapagos hotspot, *J. Geophys. Res.*, *102*, 27,341–27,354.

Canales, J. P., G. Ito, R. S. Detrick, and J. Sinton (2002), Crustal thickness along the western Galapagos Spreading Center and the compensation of the Galapagos hotspot swell, *Earth Planet. Sci. Lett.*, *203*, 311–327.

Carbotte, S. M., J. C. Mutter, and L. Xu (1997), Contribution of volcanism and tectonism to axial and flank morphology of the southern East Pacific Rise, 17°10′–17°40′S, from a study of layer 2A geometry, *J. Geophys. Res.*, *102*, 10,165–10,184.

Carbotte, S., C. Mutter, J. Mutter, and G. Ponce-Correa (1998), Influence of magma supply and spreading rate on crustal magma bodies and emplacement of the extrusive layer: Insights from the East Pacific Rise at lat 16°N, *Geology*, *26*, 455–458.

Carbotte, S. M., A. Solomon, and G. Ponce-Correa (2000), Evaluation of morphological indicators of magma supply and segmentation from a seismic reflection study of the East Pacific Rise 15°30′–17°N, *J. Geophys. Res.*, *105*, 2737–2759.

Chen, Y. J., and J. Lin (2004), High sensitivity of ocean ridge thermal structure to changes in magma supply: The Galapagos Spreading Center, *Earth Planet. Sci. Lett.*, *221*, 263–273.

Christeson, G. L., G. M. Purdy, and G. J. Fryer (1992), Structure of young upper crust at the East Pacific Rise near 9°30′N, *Geophys. Res. Lett.*, *19*, 1045–1048.

Christeson, G. L., G. M. Purdy, and G. J. Fryer (1994), Seismic constraints on shallow crustal emplacement processes at the fast spreading East Pacific Rise, *J. Geophys. Res.*, *99*, 17,957–17,973.

Christeson, G. L., G. M. Kent, G. M. Purdy, and R. S. Detrick (1996), Extrusive thickness variability at the East Pacific Rise, 9°–10°N: Constraints from seismic techniques, *J. Geophys. Res.*, *101*, 2859–2874.

Collier, J., and M. Sinha (1990), Seismic images of a magma chamber beneath the Lau Basin back-arc spreading center, *Nature*, *346*, 646–648.

Collier, J. S., and M. C. Sinha (1992), Seismic mapping of a magma chamber beneath the Valu Fa Ridge, Lau Basin, *J. Geophys. Res.*, *97*, 14,031–14,053.

Cushman, B., J. Sinton, G. Ito, and J. E. Dixon (2004), Glass compositions, plume-ridge interaction, and hydrous melting along the Galápagos Spreading Center, 90.5°W to 98°W, *Geochem. Geophys. Geosyst.*, *5*, Q08E17, doi:10.1029/2004GC000709.

DeMets, C., R. G. Gordon, D. F. Argus, and S. Stein (1990), Current plate motions, *Geophys. J. Int.*, *101*, 425–478.

DeMets, C., R. G. Gordon, D. F. Argus, and S. Stein (1994), Effect of recent revisions to the geomagnetic reversal time scale on estimates of current plate motions, *Geophys. Res. Lett.*, *21*, 2191–2194.

Detrick, R. S., P. Buhl, E. Vera, J. Mutter, J. Orcutt, J. Madsen, and T. Brocher (1987), Multi-channel seismic imaging of a crustal magma chamber along the East Pacific Rise, *Nature*, *326*, 35–41.

Detrick, R. S., A. J. Harding, G. M. Kent, J. A. Orcutt, J. Mutter, J. Orcutt, and P. Buhl (1993), Seismic structure of the southern East Pacific Rise, *Science*, *259*, 499–503.

Detrick, R. S., J. M. Sinton, G. Ito, J. P. Canales, M. Behn, T. Blacic, B. Cushman, J. E. Dixon, D. W. Graham, and J. J. Mahoney (2002), Correlated geophysical, geochemical, an volcanological manifestations of plume-ridge interaction along the Galapagos Spreading Center, *Geochem. Geophys. Geosyst.*, *3*(10), 8501, doi:10.1029/2002GC000350.

Embley, R. W., W. W. Chadwick Jr., I. R. Jonasson, D. A. Butterfield, and E. T. Baker (1995), Initial results of the rapid response to the 1993 CoAxial event: Relationships between hydrothermal and volcanic processes, *Geophys. Res. Lett.*, *22*, 143–146.

Fisher, A. T., K. Becker, T. N. Narasimham, M. G. Langseth, and M. J. Mottl (1990), Passive, off-axis convection through the southern flank of the Costa Rica Rift, *J. Geophys. Res.*, *95*, 9343–9370.

Fornari, D. J., and R. W. Embley (1995), Tectonic and volcanic controls on hydrothermal processes at the mid-ocean ridge: An overview based on near-bottom and submersible studies, in *Seafloor Hydrothermal Systems: Physical, Chemical, Biological, and Geological Interactions*, *Geophys. Monogr. Ser.*, vol. 91, edited by S. E. Humphris et al., pp. 1–46, AGU, Washington D. C.

Fornari, D. J., R. M. Haymon, M. R. Perfit, T. K. P. Gregg, and M. H. Edwards (1998), Axial summit trough of the East Pacific Rise 9°–10°N: Geological characteristics and evolution of the axial zone of fast spreading mid-ocean ridges, *J. Geophys. Res.*, *103*, 9827–9855.

Francheteau, J., R. Armijo, J. L. Cheminee, R. Hekinian, P. Lonsdale, and N. Blum (1992), Dyke complex of the East Pacific Rise exposed in the walls of Hess Deep and the structure of upper oceanic crust, *Earth Planet. Sci. Lett.*, *111*, 109–121.

Gente, P. J. M. Auzende, V. Renard, Y. Fouquet, and D. Bideau (1986), Detailed geologic mapping by submersible of the East Pacific Rise axial graben near 13°N, *Earth Planet. Sci. Lett.*, *78*, 224–236.

Hale, L. D., C. J. Morton, and N. H. Sleep (1982), Reinterpretation of seismic reflection data over the East Pacific Rise, *J. Geophys. Res.*, *87*, 7707–7717.

Harding, A. J., M. E. Kappus, J. A. Orcutt, E. E. Vera, P. Buhl, J. C. Mutter, R. Detrick, and T. Brocher (1989), The structure of young oceanic crust at 13°N on the East Pacific Rise from expanding spread profiles, *J. Geophys. Res.*, *94*, 12,163–12,196.

Harding, A. J., G. M. Kent, and A. J. Orcutt (1993), A multichannel seismic investigation of upper crustal structure at 9°N on the East Pacific Rise: Implications for crustal accretion, *J. Geophys. Res.*, *98*, 13,925–13,944.

Haymon, R. M., D. J. Fornari, M. Edwards, S. M. Carbotte, D. Wright, and K. C. Macdonald (1991), Hydrothermal vent distribution along the East Pacific Rise crest (latitude 9°09′–54′N) and its relationship to magmatic and tectonic processes on fast spreading mid-ocean ridges, *Earth Planet. Sci. Lett.*, *104*, 513–534.

Haymon, R. M., et al. (1997), Distribution of fine scale hydrothermal, volcanic and tectonic features along the EPR crest, 17°15′–18°30′S: Results of near-bottom acoustic and optical surveys, *Eos Trans. AGU*, *78*(46), Fall Meet. Suppl., F705.

Herron, T. J. (1982), Lava flow layer—East Pacific Rise, *Geophys. Res. Lett.*, *9*, 17–20.

Herron, T. J., W. J. Ludwig, P. L. Stoffa, T. K. Kan, and P. Buhl (1978), Structure of the East Pacific Rise crest from multichannel seismic reflection data, *J. Geophys. Res.*, *83*, 798–804.

Herron, T. J., P. L. Stoffa, and P. Buhl (1980), Magma chamber and mantle reflections–East Pacific Rise, *Geophys. Res. Lett.*, *7*, 989–992.

Hey, R., G. L. Johnson, and A. Lowrie (1977), Recent plate motions in the Galapagos area, *Geol. Soc. Am. Bull.*, *88*, 1404–1420.

Hooft, E. E., H. Schouten, and R. S. Detrick (1996), Constraining crustal emplacement processes from the variation in seismic layer 2A thickness at the East Pacific Rise, *Earth Planet. Sci. Lett.*, *142*, 289–309.

Hooft, E. E., R. S. Detrick, and G. M. Kent (1997), Seismic structure and indicators of magma budget along the southern East Pacific Rise, *J. Geophys. Res.*, *102*, 27,319–27,340.

Houtz, R. E. (1976), Seismic properties of layer 2A in the Pacific, *J. Geophys. Res.*, *81*, 6321–6331.

Houtz, R., and J. Ewing (1976), Upper crustal structure as a function of plate age, *J. Geophys. Res.*, *81*, 2490–2498.

Hussenoeder, S. A., J. A. Collins, G. M. Kent, R. S. Detrick, and the TERA Group (1996), Seismic analysis of the axial magma chamber reflector along the southern East Pacific Rise from conventional reflection profiling, *J. Geophys. Res.*, *101*, 22,087–22,105.

Hussenoeder, S. A., R. S. Detrick, G. M. Kent, H. Schouten, and A. J. Harding (2002a), Fine-scale seismic structure of young upper crust at 17°20′S on the fast spreading East Pacific Rise, *J. Geophys. Res.*, *107*(B8), 2158, doi:10.1029/2001JB001688.

Hussenoeder, S. A., G. M. Kent, and R. S. Detrick (2002b), Upper crustal seismic structure of the slow spreading Mid-Atlantic Ridge, 35°N: Constraints on volcanic emplacement processes, *J. Geophys. Res.*, *107*(B8), 2156, doi:10.1029/2001JB001691.

Jacobson, R. T. (1992), Impact of crustal evolution on changes of the seismic properties of the uppermost oceanic crust, *Rev. Geophys.*, *30*, 23–42.

Kappus, M. E., A. J. Harding, and J. A. Orcutt (1995), A baseline for upper crustal velocity variations along the East Pacific Rise at 13°N, *J. Geophys. Res.*, *100*, 6143–6161.

Kent, G. M., A. J. Harding, and J. A. Orcutt (1990), Evidence for a smaller magma chamber beneath the East Pacific Rise at 9°30′N, *Nature*, *344*, 650–653.

Kent, G. M., A. J. Harding, and J. A. Orcutt (1993a), Distribution of magma beneath the East Pacific Rise near the 9°03′N overlapping spreading center from forward modeling of common depth point data, *J. Geophys. Res.*, *98*, 13,971–13,995.

Kent, G. M., A. J. Harding, and J. A. Orcutt (1993b), Distribution of magma beneath the East Pacific Rise between the Clipperton Transform and the 9°17′N deval from forward modeling of common depth point data, *J. Geophys. Res.*, *98*, 13,945–13,969.

Kent, G. M., A. J. Harding, J. A. Orcutt, R. S. Detrick, J. C. Mutter, and P. Buhl (1994), Uniform accretion of oceanic crust south of the Garrett transform at 14°15′S on the East Pacific Rise, *J. Geophys. Res.*, *99*, 9097–9116.

Klitgord, K. D., and J. Mammerickx (1982), Northern East Pacific Rise: Magnetic anomaly and bathymetric framework, *J. Geophys. Res.*, *87*, 6725–6750.

Klitgord, K. D., S. P. Huestis, J. D. Mudie, and R. L. Parker (1975), An analysis of near-botom magnetic anomalies; sea-floor spreading and the magnetic layer, *Geophys. J. R. Astron. Soc.*, *43*, 387–424.

Liner, C. L. (1990), General theory and comparative anatomy of dip moveout, *Geophysics*, *55*(5), 595–607.

Luyendyk, B. P., and K. C. Macdonald (1985), A geological transect across the crest of the East Pacific Rise at 21°N latitude made from the deep submersible Alvin, *Mar. Geophys. Res.*, *7*, 467–488.

Macdonald, K. C., and P. J. Fox (1988), The axial summit graben and cross-sectional shape of the East Pacific Rise as indicators of axial magma chambers and recent volcanic eruptions, *Earth Planet. Sci. Lett.*, *88*, 119–131.

McClain, J. S., J. A. Orcutt, and M. Burnett (1985), The East Pacific Rise in cross section: A seismic model, *J. Geophys. Res.*, *90*, 8627–8640.

McDonald, M. A., S. C. Webb, J. A. Hildebrand, and B. D. Cornuelle (1994), Seismic structure and anisotropy of the Juan de Fuca Ridge at 45°N, *J. Geophys. Res.*, *99*, 4857–4873.

Morton, J. L., and N. Sleep (1985), Seismic reflections from a Lau Basin magma chamber, in *Geology and Offshore Resources of Pacific Island Arcs–Tonga Region*, *Earth Sci. Ser.*, vol. 2, edited by D. W. Scholl and T. L. Vallier, pp. 441–453, Circum-Pac. Counc. for Energy and Miner. Resour., Houston, Tex.

Morton, J. L., N. H. Sleep, W. R. Normark, and D. H. Tompkins (1987), Structure of the Southern Juan de Fuca Ridge from seismic reflection records, *J. Geophys. Res.*, *92*, 11,315–11,326.

Mutter, J. C., S. M. Carbotte, W. Su, L. Xu, P. Buhl, R. S. Detrick, G. M. Kent, J. A. Orcutt, and A. J. Harding (1995), Seismic images of active magma systems beneath the East Pacific Rise between 17°05′ and 17°35′S, *Science*, *268*, 391–395.

Pan, Y., and R. Batiza (2003), Magmatic processes under mid-ocean ridges: A detailed mineralogic study of lavas from East Pacific Rise 9°30′N, 10°30′N, and 11°20′N, *Geochem. Geophys. Geosyst.*, *4*(11), 8623, doi:10.1029/2002GC000309.

Perfit, M. R., D. J. Fornari, M. C. Smith, J. F. Bender, C. H. Langmuir, and R. M. Haymon (1994), Small-scale spatial and temporal variations in mid-ocean ridge crest magmatic processes, *Geology*, *22*, 375–379.

Phipps Morgan, J., and Y. J. Chen (1993), Dependence of ridge-axis morphology on magma supply and spreading rate, *Nature*, *364*, 706–708.

Purdy, G. M., L. S. L. Kong, G. L. Christeson, and S. C. Solomon (1992), Relationship between spreading rate and the seismic structure of mid-ocean ridges, *Nature*, *355*, 815–817.

Rohr, K. M. M., B. Milkereit, and C. J. Yorath (1988), Asymmetric deep crustal structure across the Juan de Fuca Ridge, *Geology*, *16*, 533–537.

Singh, S. C., G. M. Kent, J. S. Collier, A. J. Harding, and J. A. Orcutt (1998), Melt to mush variations in crustal magma properties along the ridge crest at the southern East Pacific Rise, *Nature*, *394*, 874–878.

Sinton, J. M., and R. S. Detrick (1992), Mid-ocean ridge magma chambers, *J. Geophys. Res.*, *97*, 197–216.

Sinton, J., R. Detrick, J. P. Canales, G. Ito, and M. Behn (2003), Morphology and segmentation of the western Galapagos spreading center, 90.5°–98°W: Plume-ridge interactions at an intermediate spreading ridge, *Geochem. Geophys. Geosyst.*, *4*(12), 8515, doi:10.1029/2003GC000609.

Tivey, M. A. (1994), Fine-scale magnetic anomaly field over the southern Juan de Fuca Ridge: Axial magnetization low and implications for crustal structure, *J. Geophys. Res.*, *99*, 4833–4855.

Tivey, M. A., and H. P. Johnson (1993), Variations in oceanic crustal structure and implications for the fine scale magnetic anomaly signal, *Geophys. Res. Lett.*, *20*, 1879–1882.

Tolstoy, M., A. J. Harding, and J. A. Orcutt (1997), Deepening of the axial magma chamber on the southern East Pacific Rise toward the Garrett Fracture Zone, *J. Geophys. Res.*, *102*, 3097–3108.

Toomey, D. R., G. M. Purdy, S. C. Solomon, and W. S. D. Wilcock (1990), The three-dimensional seismic velocity structure of the East Pacific Rise near latitude 9°30′N, *Nature*, *347*, 639–645.

Turcotte, D. L., and G. Schubert (1982), *Geodynamics: Applications of Continuum Physics to Geological Problems*, 450 pp., John Wiley, Hoboken, N. J.

Vera, E. E., and J. B. Diebold (1994), Seismic imaging of oceanic layer 2A between 9°30′N and 10°N on the East Pacific Rise from two-ship wide-aperture profiles, *J. Geophys. Res.*, *99*, 3031–3041.

Vera, E. E., J. C. Mutter, P. Buhl, J. A. Orcutt, A. J. Harding, M. E. Kappus, R. S. Detrick, and T. M. Brocher (1990), The structure of 0- to 0. 2-m.y.-old oceanic crust at 9°N on the East Pacific Rise from expanding spread profiles, *J. Geophys. Res.*, *95*, 15,529–15,556.

Wilcock, W. S. D., G. M. Purdy, S. C. Solomon, D. L. DuBois, and D. R. Toomey (1992), Microearthquakes on and near the East Pacific Rise, 9°–10°N, *Geophys. Res. Lett.*, *19*, 2131–2134.

Zelt, C. A., and R. B. Smith (1992), Seismic travel time inversion for 2-D crustal velocity structure, *Geophys. J. Int.*, *108*, 16–34.

T. M. Blacic, Department of Geology, University of California at Davis, 1 Shields Avenue, Davis, CA 95616, USA. (blacic@geology.ucdavis.edu)

J. P. Canales and R. S. Detrick, Department of Geology and Geophysics, Woods Hole Oceanographic Institute, Woods Hole, MA 02543, USA.

G. Ito and J. Sinton, School of Ocean and Earth Science and Technology, University of Hawaii, Honolulu, HI 96822, USA.

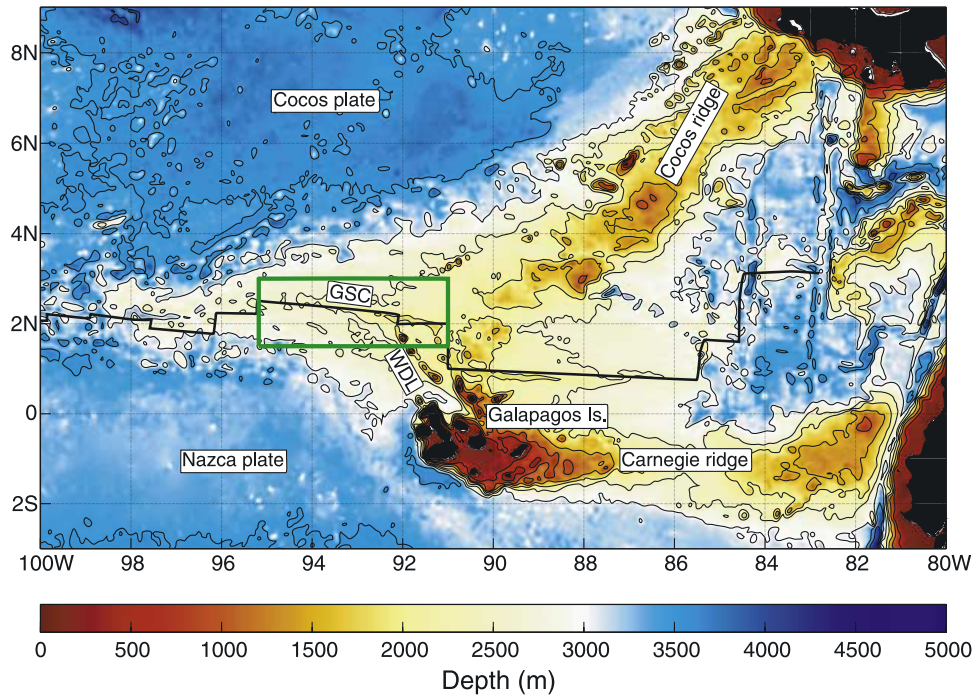

Figure 1. Map of the Galapagos region in the western equatorial Pacific. The MCS survey of the Galapagos Plume–Ridge Interaction Multidisciplinary Experiment (G-PRIME) focused on the western Galapagos Spreading Center (GSC) indicated by the green box. Black lines indicate location of ridge segments and transform faults. WDL is the Wolf-Darwin lineament. Contours are every 500 m. (After *Canales et al.* [2002], reprinted with permission from Elsevier Science.)

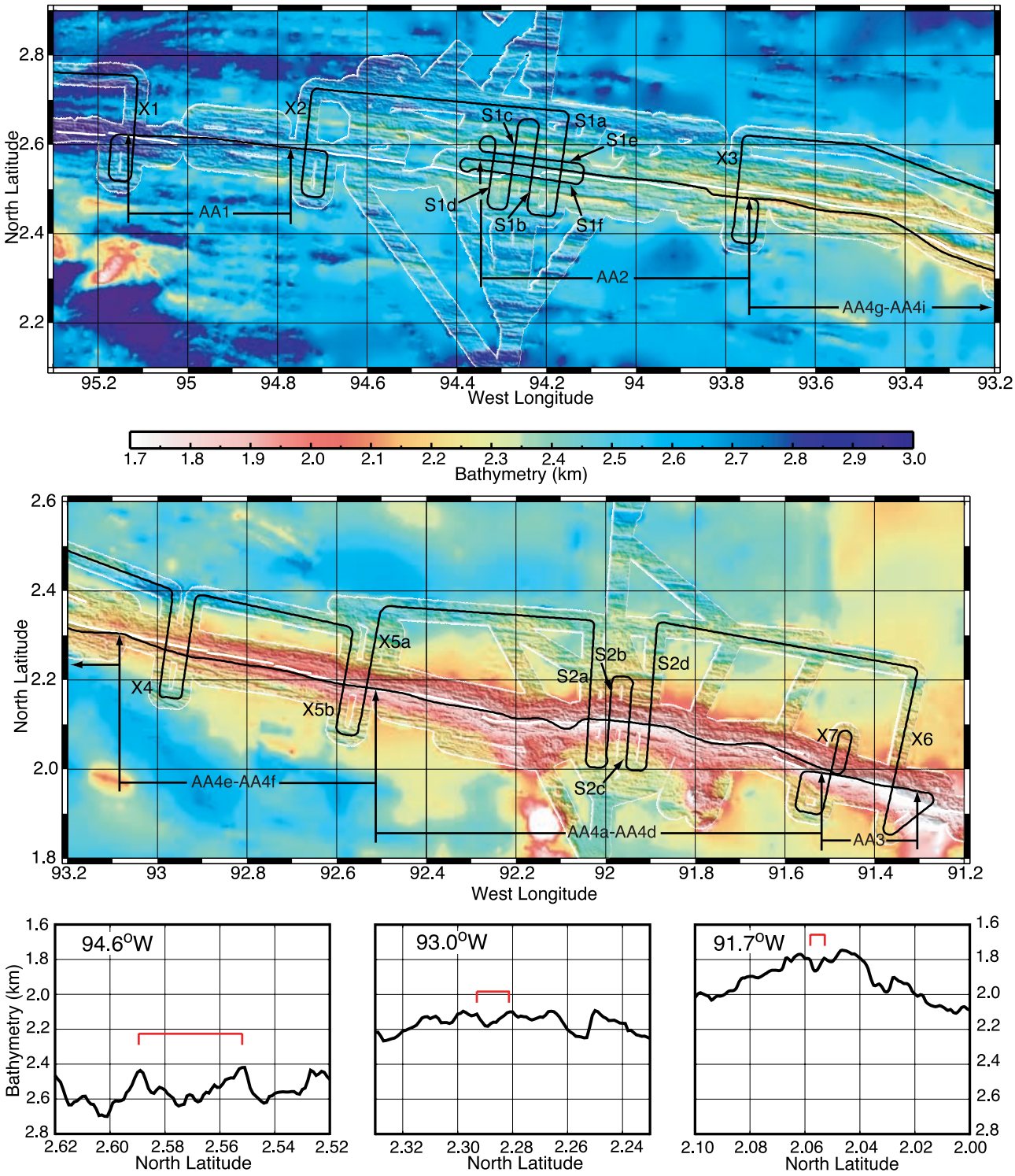

Figure 2. (top and middle) Bathymetry maps of the western Galapagos Spreading Center showing the location of the multichannel seismic reflection lines. (bottom) Bathymetry profiles showing cross sections of the ridge axis at 94.6°W, 93.0°W, and 91.7°W. A prominent axial high exists east of ~92.5°W. From ~92.7° to 95.3°W the ridge axis shows transitional topography lacking both an axial high and an axial valley. Red brackets indicate width of axial trough.

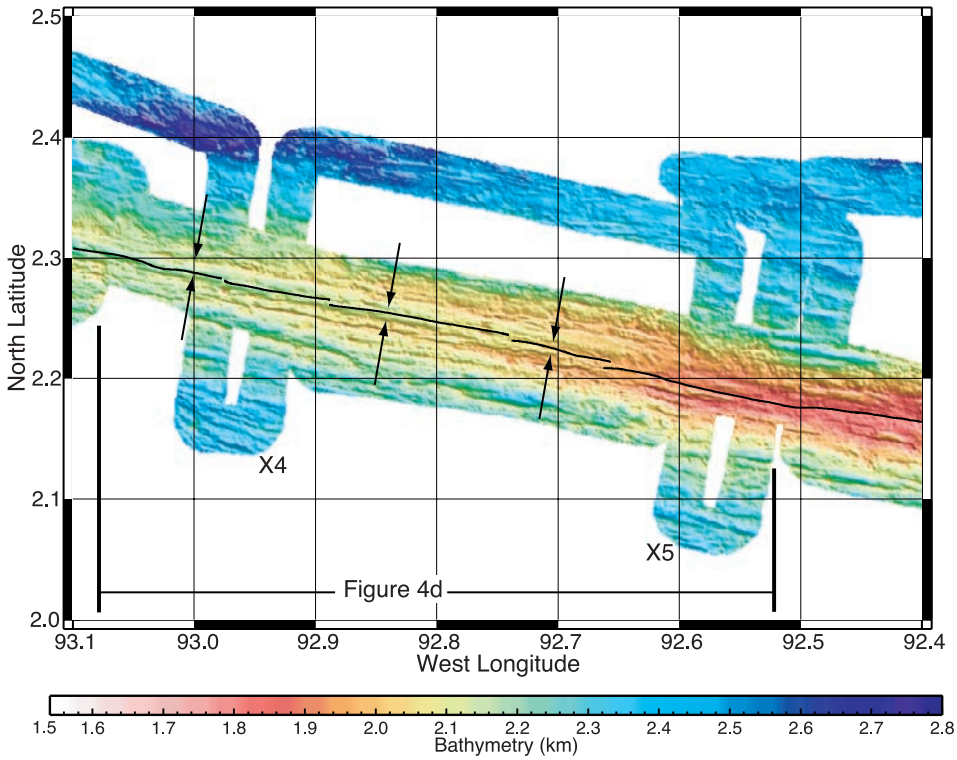

Figure 7. Bathymetry map of GSC showing the region where a prominent axial trough appears and the axial high disappears. Black line marks the location of the ridge axis [*Sinton et al.*, 2003]. Black arrows indicate the approximate bounds of the axial trough. Bold vertical lines indicate extent of line AA4e, Figure 4d.